



# Assessment of tropospheric ozone products from downscaled CAMS reanalysis and CAMS daily forecast using urban air quality monitoring stations in Iran

Najmeh Kaffashzadeh<sup>1</sup> and Abbas Ali Aliakbari Bidokhti<sup>1</sup>

5 <sup>1</sup> Institute of Geophysics, University of Tehran, Tehran, Iran

*Correspondence to:* Kaffashzadeh Najmeh (najmeh.kaffashzadeh@gmail.com)

**Abstract.** Tropospheric ozone time series consist of the effects of various scales of motion, from meso to large timescales, which is often challenging for global models to capture. This study uses two global datasets, namely the reanalysis and daily forecast of the Copernicus Atmospheric Monitoring Service (CAMS), to assess the capability of these products in presenting  
10 ozone's features on regional scales. We obtained 17 relevant meteorological and several pollutant species, such as O<sub>3</sub>, CO, NO<sub>x</sub>, etc., from CAMS. Furthermore, we employ in situ measured ozone at 27 urban stations over Iran for the year 2020. We decompose the datasets into three spectral components, i.e., short (S), medium (M), and long (L) terms. To cope with the scaling issue between the measured data and the CAMS' products, we downscale the datasets using a Long Short-Term Memory (LSTM) neural network. We only evaluate the S and M terms of the models against those of the observed datasets  
15 for all stations. Results show correlation coefficients larger than 0.7 for S and about 0.95 for M in both models. It turns out that both datasets demonstrate more correspondence precision for the M component than that for the S. The performance of the models varies across cities, for example, the highest error is for areas with high emissions of O<sub>3</sub> precursors. The robustness of the results is confirmed by performing an additional downscaling method.

## 1 Introduction

20 Near-surface ozone (O<sub>3</sub>), or tropospheric ozone at ground level, is a secondary air pollutant that deteriorates human health and plants via damaging respiratory systems (Bell et al., 2006; Fowler et al., 2009; Mills et al., 2011; Malley et al., 2015). Exposure to high concentrations of air pollution, especially O<sub>3</sub>, leads to premature deaths, in particular for those suffering from asthma disease. Many efforts have been made to study ozone and its precursors in Iran, which suffers from severe ambient air  
25 (2017) reported a total of 1363 premature deaths attributed to O<sub>3</sub> in Tehran within three years, 2013–2016. Long-term exposures to ambient O<sub>3</sub> are responsible for 173 deaths from respiratory disease in Ahvaz for the year 2012 (Goudarzi et al., 2015).



Ozone is either transported naturally from the stratosphere or produced in situ by photochemical oxidation of ozone's precursor gases such as nitrogen oxides ( $\text{NO}_x$ ), non-methane volatile organic compounds (NMVOC), methane ( $\text{CH}_4$ ), or carbon monoxide (CO) in the presence of sunlight (Crutzen 1974; Monks et al., 2015; Cooper et al., 2014). The ozone level is not only a function of its precursor's emissions but also of meteorological conditions that influence the evolution of emissions and photochemical products (Bloomer et al., 2009; Li et al., 2020). It has been shown that not only local emissions and winds but also synoptic conditions control the ozone levels over Iran (Borhani et al., 2021; Zohdirad et al., 2022; Jafari Hombari and Pazhoh, 2022). Several synoptic systems, which cause the high levels of ozone over Tehran, have been recognized and classified in a study by Khansalari et al. (2020) and Lashkari et al. (2020).

Reanalysis data provides a global picture of past weather and climate. These data are constructed by combining atmospheric observations such as satellite, radar, and in situ measurements with a detailed computer simulation of the atmosphere, using data assimilation technique. Reanalysis data have been widely used as an initial condition for the daily forecast of the atmosphere or boundary conditions in regional models, for the study of climate change, and as proxies to complement insufficient in situ measurements. In recent years, the Copernicus Atmosphere Monitoring Service (CAMS) has been mainly developed to assimilate the chemical compositions such as tropospheric ozone and aerosol concentrations, but it also holds outputs for several meteorological variables (Innes et al., 2019). Several studies have evaluated CAMS reanalysis (hereafter CAMSRA) products and compared them with other reanalysis datasets and a control run (no assimilation). As an example, an intercomparison of tropospheric ozone from seven reanalysis datasets in East Asia has reported that CAMSRA depicts more reasonable spatial-temporal variability than other datasets (Park et al., 2020). They also show the suitability of CAMSRA for the study of local tropospheric ozone on seasonal to interannual timescales but the inadequacy of that to study long-term trends. Results of the study by Huijnen et al. (2020) reveal the ability of CAMSRA to reproduce background  $\text{O}_3$  in terms of mean and variability on various timescales such as synoptic, seasonal, etc. Several studies mention that the performance of CAMSRA differs depending on the region (Wang et al., 2020; Wagner et al., 2021). For instance, it has been shown that there is more agreement between CAMSRA and observations over Europe than in the Tropics (Errera et al., 2021). CAMS also provides daily forecasts (hereafter CAMSFC), which have a finer horizontal resolution and a larger number of vertical model levels than CAMSRA. System upgrades and verifications of CAMSFC are reported in several studies (Schulz et al., 2021; Eskes et al., 2021). A recent validation based on various observations shows that, in terms of bias, CAMSFC overestimates surface ozone values at most of the stations (Sudarchikova et al., 2021). However, it shows significant correlations across most of the stations, e.g., in China.

Despite many evaluation studies of CAMSRA and CAMSFC in different parts of the globe, less attention has been given so far to Iran, which is a country with a complex topography and diverse meteorological systems that contribute to the ozone level in this area. This study aims to address two questions: (1) how are the performances of CAMSRA and CAMSFC in simulating ozone over this region? (2) To what extent can downscaled CAMS datasets be used to study surface ozone at a city scale? To compensate for the limited spatial resolutions of the models, we downscale the CAMS ozone using the Long Short-Term Memory (LSTM) technique. The data are compared with the measured ozone data at 27 air quality monitoring



stations distributed over different parts of the country. That allows us to assess the CAMS over diverse zones, e.g., a highly populous and polluted area vs. a small and desert-like town.

65 A detailed description of the datasets used in this study is presented in Sect. 2. The methodology is explained in Sect. 3, and the results are shown in Sect. 4. The discussion is presented in Sect. 5, and the paper ends with the conclusion's remarks in Sect. 6.

## 2 Description of Data

### 2.1 CAMS products

70 This study uses two data products, namely CAMSRA and CAMSFC, that have been produced by the ECMWF in the framework of the CAMS. These datasets specific to tropospheric ozone analysis are introduced in the following subsections. An overview of the main differences and similarities between both products is given in Table 1. For more details on other aspects, the reader is referred to the references.

#### 2.1.1 CAMS reanalysis (CAMSRA)

75 This product is the latest (state-of-the-art) global CAMS reanalysis dataset of atmospheric compositions. They are produced using four-dimensional variation (4D-Var) as an assimilation technique. The chemistry module of the CAMS relies on the IFS(CB05) tropospheric chemistry mechanism with 52 species and 130 reactions (Huijnen et al., 2010; Flemming et al., 2015; Huijnen et al., 2020). Dry deposition velocities are derived from the SUMO model (Michou et al., 2004). Anthropogenic emissions are based on the MACCity inventory (Granier et al., 2011), with modified wintertime CO emissions over North America and Europe (Stein et al., 2014). Monthly mean biogenic VOC emissions are derived offline from MEGAN (Guenther et al., 2006), using NASA's Modern-Era Retrospective Analysis for Research and Applications (MERRA) reanalyzed meteorological fields (Sindelarova et al., 2014). Daily biomass-burning emissions originating from the Global Fire Assimilation System, version 1.2 (GFASv1.2, Kaiser et al., 2012) are inferred from satellite observations of fire activities. The meteorological model consists of the given version of the Integrated Forecast System (IFS), i.e., CY42R1, with an interactive ozone and aerosol radiation scheme. It is noteworthy that newer versions of data have been frequently adopted in CAMS.  
80 Comparing to the previous atmospheric chemistry CAMS reanalysis data, CAMSRA has a finer horizontal resolution of 80 km with 60 vertical model levels, with the top level at 0.1 hPa. CAMSRA covers data for the period of January 2003 to December 2021. The data are archived in 3 hourly time intervals. Hereafter, the ozone from this dataset is called O<sub>3</sub><sup>RA</sup>.

#### 2.1.2 CAMS forecast (CAMSFC)

90 In addition to the aforementioned datasets, CAMSFC issues (and produces) a daily global forecast of atmospheric compositions twice a day, which is initialized from analysis at 00:00 and 12:00 UTC. The forecast consists of more than 50 chemical species



and seven different aerosols. It provides outputs for several meteorological variables as well. Compared to CAMSRA, in CAMSFC only the initial conditions of each forecast are obtained from reanalysis datasets, i.e., combining the previous forecasts with satellite observations using the 4D-VAR data assimilation technique. CAMSFC uses an atmospheric model to determine the evolution of the concentration of all species over time for the next five days. Apart from the required initial state, it also uses inventory-based or observation-based emissions estimates as boundary conditions at the surface. Biogenic emissions originate from CAMS-GLOB-BIO v1.1, which is calculated from the MEGAN v2.1 model using ERA-Interim meteorology (Sindelarova et al., 2022). Monthly average of anthropogenic emissions is derived from the CAMS\_GLOB\_ANT v2.1 inventory based on a combination of EDGAR v4.3.2x and CEDS emissions (Granier et al., 2019). Biomass burning injects from GFAS. Dry depositions of trace gases are calculated online. Sulfur species, nitrate, and ammonium are coupled between chemistry and aerosol schemes. In contrast to the CAMSRA, CAMSFC is available at a finer horizontal resolution of 40 km. CAMSFC is upgraded regularly, e.g., once a year, during which the model's resolution can change or new species can be added. From 9 July 2019, CAMSFC uses the assimilation system's IFS CY46R1, in which the vertical model levels have been upgraded from 60 to 137. Details of other upgrades to this system can be found in Haiden et al. (2019) and Basart et al. (2019). IFS CY47R1 was used on 6 October 2020, with some upgrades in observations, emissions, and model changes (Eskes et al., 2021; Sudarchikova et al., 2021). The temporal coverage of the CAMSFC is from 2015 to the present, with temporal resolutions of 1 hourly (only for surface fields) and 3 hourly. This study uses 3 hourly forecast fields from 00:00 UTC up to 24 hours. Hereafter, the ozone from this dataset is called  $O_3^{FC}$ .

## 2.2 In situ measurement datasets

Surface-based measurements of ozone were extracted from the Tehran air quality control portal, which is publicly available, for 21 stations. A couple of the stations contain no data records, and the data sparsity at the stations differs from year to year. Hourly time series of surface ozone for other cities are not accessible to the public. They were obtained from the Iranian Environmental Protection Organization for 54 air quality monitoring stations. We added the Geophysics station, which is located at the Geophysics Institute, University of Tehran, Tehran. This station measures surface ozone along with several other variables such as air temperature, nitrogen oxides, wind, total ozone column, etc. Most of the air quality monitoring stations in Iran are installed in the cities, as they are aimed for the public health report. There is no information about stations' type or availability of the data at background sites. To have a common quality, the validity of the data was checked by performing a few statistical tests, such as (1) range test: verifies if the values are within the acceptable range limits (Zahumensky, 2004; Taylor and Loescher, 2013); (2) constant value test: checks the required variability among successive values (Zahumensky, 2004); and (3) discontinuity test: identifies suspicious data points before and ahead of the discontinuities (Zurbenko et al., 1996; Gerharz et al., 2011). We use the stations containing data for the year 2020, where more than 50 % of the data is available for each month. Table A1 lists the names and geographical locations of the stations, of which the first 22 are ordered based on the stations' latitudes. In Table A1, there is a number along with the stations' names, hereafter, the stations are referred with



these numbers. To include more stations in the analysis, we consider five more stations in Table A1, i.e., from 23 to 27, which only one or two months of the year 2020 contain less than 50 percent of data (see Figure A1). The distribution of the stations is shown in Fig. 1, which covers three large cities (Tehran, Shiraz, and Tabriz) and six small cities (Birjand, Gilan, Hamedan, Zanjan, Markazi, and Yazd). Hereafter, the observation datasets and observed ozone are called OBS and  $O_3^{OBS}$ , respectively. Both reanalysis datasets were co-located with OBS through temporal and spatial interpolations. OBS data are available in hourly resolution, in contrast to the CAMS datasets that are available in 3 hourly intervals. To match the frequency of the CAMS outputs with OBS, 3 hourly observed values are considered in such a way that at least two hourly values are available; otherwise, it renders the value as missing.

### 3 Methodology

#### 3.1 Spectral decomposition of the time series

The presence of various scales of motion, which are caused by several physical and chemical processes, in the time series of  $O_3$  can complicate the analysis and interpretation of data. As an example, short-term and fast fluctuations in the  $O_3$  time series are majorly attributed to chemical processes such as NO titration, whereas long-term and seasonal variation is mainly related to solar radiation. Scale analysis is a method by which the time series can be separated into different temporal terms. Here, the time series of  $O_3$  is decomposed into three different spectral components, namely short (period less than 2 days), medium (period of 2–21 days), and long (periods longer than 21 days) terms, by applying the Kolmogorov-Zurbenko (KZ) technique (Rao et al., 1997). KZ is essentially a low-pass filter that consists of repeated moving averages. Its use has been demonstrated in earlier studies (Hogrefe et al., 2000; Kang et al., 2013; Seo et al., 2014). A detailed discussion of the KZ filter along with a comparison to other separation techniques can be found in Eskridge et al. (1997) and Loneck and Zurbenko (2020). KZ requires two input parameters, KZ ( $m, k$ ), where  $m$  is the window size for filtering and  $k$  is the number of iterations. Since the values that have been commonly used for  $m$  and  $k$  in the literature may not be applicable for 3-hourly data, we selected them based on the criteria suggested in Yang and Zurbenko (2010):

$$m \times \sqrt{k} \leq p \quad (1)$$

KZ filters out all periods that are less than  $p$ , i.e., the number of filtered time intervals. Therefore, three components of interest in this study are estimated as follows:

$$S = O - KZ(5, 5) \quad (2)$$

$$M = KZ(5, 5) - KZ(35, 5) \quad (3)$$

$$L = KZ(35, 5), \quad (4)$$

where  $O$  refers to the original time series and  $S, M,$  and  $L$  indicate the short, medium, and long terms, respectively. Here, the units of  $O$  and the spectral terms are in  $\text{nmol mol}^{-1}$ .



### 3.2 Statistical downscaling

To bridge the spatial scaling issue between coarse resolution CAMS datasets and local-scale measured data, statistical  
155 downscaling (SD) methods have been developed (Wilby and Wigley, 1997). SD refers to the use of statistical-based techniques  
to determine a relationship between global scale models' outputs and observed local (small) scale variables (Wilby et al., 2004;  
Wilby and Dawson, 2013). There are numerous SD methods such as linear regression (Sachindra et al., 2013; Beecham et al.,  
2014), stochastic weather generators (Wilks, 1999; Kilsby et al., 2007; Semenov and Stratonovitch, 2010), and artificial neural  
networks (Tripathi et al., 2006; Ahmed et al., 2015; Sachindra et al., 2018; Sebbar et al., 2023), to name a few. In this study, a  
160 deep learning method known as LSTM network was used to analyze the complex relationship between O<sub>3</sub> and its precursors.  
LSTM is a modified version of a recurrent neural network designed to handle long-term (and short-term) dependencies in  
sequential data (Hochreiter and Schmidhuber 1997). LSTM contains memory cells that can hold (store) information for a long  
time, making them suitable for time series analysis. The standard LSTM consists of three gates as input, forget, and output  
gates for controlling movement of information. We use Keras, a high-level neural network Python library ("Keras: the Python  
165 Deep Learning library", Chollet, 2015; <https://keras.io>) to build and train the LSTM models. This model requires a specific  
configuration and tuning to work effectively with the datasets. A range of control values was tested by multiple trial-error  
evaluations using the Scikit function GridSearchCV. The most effective (optimum) hyperparameters are listed in Table A2.  
Several meteorological variables were selected from CAMSRA and CAMSFC products, as listed in Table A3. A cross-  
validation Lasso regression was performed to identify the potential predictors. The concentration of O<sub>3</sub> is not only affected by  
170 meteorological factors but also by the influence of the O<sub>3</sub> level in the past. A partial autocorrelation function was utilized to  
estimate the correlation between observed O<sub>3</sub> at time T and earlier time steps. For most of the stations, the autocorrelation  
coefficients decrease after a time lag of 24 hours within a confidence interval of 95 %. So, the observed O<sub>3</sub> at times T-1, ...,  
and T-8 were also considered predictors at each station. Selected predictors and observed O<sub>3</sub> were decomposed using Eq. (2),  
(3), and (4). In order to provide the final output, the LSTM architecture was trained on all decomposed datasets. The data  
175 records were divided into 65 % for the training subset and the rest (35 %) for the validation subset. The best model was chosen  
based on the R<sup>2</sup> score (coefficient of determination). The selected model was applied to all data records to provide a downscaled  
output. All these procedures are illustrated in Fig. 2.

### 3.3 Model evaluation

We use the mean square error (MSE) as a metric to evaluate the models' performance. The MSE is defined as the squared  
180 mean of the difference between modelled ( $x_m$ ) and observed ( $x_o$ ) variables.

This metric can be modified to include all relevant model evaluation indicators, i.e., bias, variance, and correlation, as (Murphy,  
1988; Solazzo and Galmarini, 2016):

$$MSE = (\bar{x}_m - \bar{x}_o)^2 + (\sigma_m - r \sigma_o)^2 + \sigma_o^2(1 - r^2) \quad (5)$$



185 where  $\sigma_m$  and  $\sigma_o$  refer to the standard deviation of the modelled and observed data, respectively, and  $r$  is the coefficient of correlation between the observed and assimilated datasets. In Eq. (5), the first term (hereafter E1) shows the deviation between average modelled ( $\bar{x}_m$ ) and measured ( $\bar{x}_o$ ) datasets and refers to the model accuracy. The second term (hereafter E2) contains the variance error, i.e., the discrepancy in amplitude or phase between the variability of the modelled and observed values, that determines the precision of the model. Also, the third part (hereafter E3) refers to unsystematic errors related to the associativity between observed and assimilated datasets. In other words, the E2 indicates an explained error, which reveals the variance error arising from the variability of the modelled variables that are not observed in measurements. The E3 represents an unexplained error, reflecting the lack of observed variability in the modelled data. Due to the spectral decomposition of the data, the S and M components have zero mean fluctuations. Hence, the E1 term in Eq. (5) is zero, and only the E2 and E3 terms are analyzed below.

195 To compare the distribution of error of modeled  $O_3$  before and after downscaling, the skill score (SS) is calculated as (Wilks, 2006)

$$SS = 1 - \frac{MSE}{MSE_{ref}}$$

200 Here,  $MSE_{ref}$  and  $MSE$  refer to the MSE of  $O_3^{RA}$  (or  $O_3^{FC}$ ) and downscaled  $O_3$  ( $O_3^{SD}$ ), respectively. The value of SS varies between 0 and 1. The value is zero once there is no preference in  $O_3^{SD}$  with respect to  $O_3^{RA}$  (or  $O_3^{FC}$ ), i.e., the  $O_3$  variability is not explained by selected predictors. The value of SS is one when the MSE of  $O_3^{SD}$  is zero, which means the whole  $O_3$  variability in the LSTM model is explained by the predictors, i.e., the LSTM model is perfect.

## 4 Results

### 4.1 Spectral components

205 The time series of  $O_3$  and all meteorological variables for OBS and CAMS datasets decompose into three spectral components, short (S), medium (M), and long (L), by applying the method (KZ filter) explained in Sect. 3.1. Figure 3 shows the original time series of  $O_3^{OBS}$ ,  $O_3^{RA}$ , and  $O_3^{FC}$  and their estimated spectral components at the first station. To clearly see the signals, we only show part of the time series, here for the summer months (June, July, and August: JJA). Looking at the original 3 hourly time series (Fig. 3a), both CAMS datasets overestimate and underestimate ozone during different periods, but it is difficult to determine any clear patterns or identify specific reasons for the model bias. The S component contains frequent fast oscillations occurring every day with regular maxima and minima (see Fig. 3b). In this figure, the amplitude of S oscillations of the  $O_3^{RA}$  and  $O_3^{FC}$  is different from that in OBS, indicating differences in the diurnal cycle of observed and simulated ozone mixing ratios. The M term captures variability on the timescale of synoptic systems. Some episodic events are more visible in the M component than in the S component. For instance, in Fig. 3c, the M component of the OBS represents a clear signal of an episodic event in the middle of June. This episode is not well captured in CAMSRA while it is captured in CAMSFC. It seems that for most of the periods, the variations of the M component in both CAMS datasets are in good agreement with those in



215 OBS, while the amplitudes of oscillations in CAMS do not correspond well with those in OBS. The underestimation and  
overestimation of the amplitude (with respect to observations) in CAMSFC is less than that in CAMSRA. Compared to the S  
and M terms, which oscillate around zero, the mean values of the L components are not zero (see Fig. 3d). The L represents  
variations of the ozone mixing ratios on seasonal, semi-seasonal, and multiannual timescales. Comparing the variations of  
CAMSRA and CAMSFC with OBS for L shows more similarity between CAMSFC and OBS than between CAMSRA and  
220 OBS. Both models exhibit a high bias with respect to the ozone mixing ratios. Nevertheless, the decomposition of the L  
component is not reliable due to the limited period (one year) of the available data, so hereafter we only assess the S and M  
components.

#### 4.2 Variable selections

The data for 17 relevant meteorological variables was extracted from CAMS products. To avoid model overfitting, we identify  
225 potential predictors of variables. The relationships between predictors and  $O_3$  were estimated by performing LASSO (Least  
Absolute Shrinkage and Selection Operator) regression. The variables with high feature importance were considered for use  
in the LSTM modeling. Table 2 lists selected predictors for both components of CAMSRA. At station 1, twelve variables,  
namely, T, V, U10m, V10m, MSLP, SP, T2m, SH, W, CO,  $NO_2$ , and  $O_3^{RA}$ , are identified as the potential predictors of the S  
component, while four variables, i.e., U10m, W,  $SO_2$ , and  $O_3^{RA}$ , are selected for the M term. Some of the selected predictors  
230 are common between the S and M components. A few meteorological variables such as T2m, SP, MSLP, W, and U10m (or  
V10m) appear for the S component at most of the stations. These variables reflect the information about temperature, pressure,  
and vertical velocity. Temperature is one of the key meteorological factors influencing on the S term variability of  $O_3$  through  
its effect on the biogenic emissions, photochemical kinetics reaction rate, and anthropogenic emissions. Stable anticyclones  
and sunny conditions promote  $O_3$  formation and accumulation. Zonal and meridional winds at 10 meters are important for the  
235 dispersion of ozone precursors at local scales. For most of the station, the S term is affected by pollutant species such as  $O_3^{RA}$ ,  
 $NO$ , and  $NO_2$ , of which  $NO$  and  $NO_2$  are recognized as potential drivers of  $O_3$  levels. Selection of TCC and FCC for the M  
component at most stations indicates that cloud covers are mostly associated with synoptic systems (e.g., occurrence of high  
pressure systems associated with clear-sky conditions) and  $O_3$  variability on this scale. The M component at a few stations,  
e.g., 4, 6, 9, 13, etc., shows weak associations with the parameters, so no variables are selected for them. This situation often  
240 happens for the M component and suggests the role of other factors (not included in the predictors). Similar to the CAMSRA,  
for the CAMSFC the number of selected parameters for the S is larger than that for the M (see Table A4). In CAMSFC, BLH  
and V10m (or U10m) appear as dominant meteorological drivers affecting the S component. The M term is mostly associated  
with  $O_3^{FC}$ .

#### 4.3 LSTM model and validation





245 The LSTM model was trained and validated with the datasets, as explained in Sect. 3.2. The model was performed using  
several epochs from 1 to 30. The best model was selected based on the  $R^2$  score (coefficient of determination), which indicates  
the amount of explained variability by the LSTM model. Figure 4 shows the  $R^2$  of the selected model for all data series at each  
station. Their associated epoch numbers are listed in Table A5. For most of the datasets, the  $R^2$  is larger than 0.5, indicating  
that more than 50 % of the  $O_3$  variability is explained by the LSTM. The  $R^2$  for the M component is larger than that for the S  
250 term, despite the smaller number of predictors for the M. That might reflect that the more predictors, the better the model  
would not be. In this figure, the  $R^2$  of the M is around 0.9 for all stations, while it varies for the S term. The  $R^2$  value of the S  
at the stations over the city of Tehran is within the same range of 0.6 to 0.8. Both CAMSRA and CAMSFC show the  $R^2$  less  
than 0.5 for the S term of a few stations, namely 1, 2, 3 (Tabriz), 22 (Yazd), and 24 (Zanjan). A possible reason for that could  
be the peculiar characteristics of short-term ozone variability at these sites or their geographical locations.

255 Figure 5 shows the box plots of MSE and different terms of MSE, i.e., E2, E3, for both components of  $O_3^{SD}$ . For the sake of  
simplicity, descriptions of the results are mostly based on the mean values. Nevertheless, the values of the indicators at each  
station are shown as a scatter point next to the box plots. From Fig. 5a, it turns out that the mean MSE (shown with red squares)  
of  $O_3$  for the S component is larger than that for the M component for both models. In other words, there is a better agreement  
between the M components of OBS and CAMS than the S components. That might arise from the larger variability of S than  
260 M (see Fig. 3). The differences between the mean MSE of CAMSRA and CAMSFC are tiny, so both models show similar  
performance. Low values of the MSE for CAMSRA\_S and CAMSFC\_S are attributed to stations 22 (Yazd), 20 (Hamedan),  
and 24 (Zanjan). On the other hand, the largest value of the MSE is associated with the  $O_3^{SD}$  of the stations located in the city  
of Tehran. The stations in the northern part of the city (e.g., stations 4, 5, 6, 7, 8, and 9) show larger MSE than the stations in  
the southern part (e.g., stations 11, 12, 14, 15, 16, 17, 18, and 19). The large value of MSE is also found for the S term at the  
265 stations located in Shiraz and Tabriz, which are known as big and highly populated cities in Iran. Station 2 in Tabriz shows  
less MSE than stations 1 and 3, which are located in the industrialized part of the city. Fig. 5b shows the explained error (E2)  
in CAMSRA and CAMSFC for both components. E2 is a model related error, a possible source for this can be a  
misrepresentation of short- and meso-scale phenomena in models. The small values of E2 reflect the low contributions of E2  
to the MSE and the noticeable improvement of the  $O_3^{SD}$  (via downscaling procedures). The major portions of the MSE are  
270 associated with the unexplained errors (E3) for both components, see Fig. 5c. The E3 for the S component is larger than that  
for M, as expected from the variance of these components. A large value of E3 for the S component can arise from the CAMS'  
deficiency in resolving the meso-scale phenomena such as local winds, NO titration, and their influences on  $O_3$  variability.  
Assessing the element of E3 (see the third term of Eq. (5)) shows that large variances of observations ( $\sigma_o$ ) or small correlations  
( $r$ ) cause the large E3 and consequently the large MSE. Fig. A2a shows the correlation between the models and observation  
275 datasets for both components. This figure shows that M contains a larger correlation ( $r > 0.9$ ) than S in both models. A high  
value of correlation between two terms can be attributed to the larger covariance of two terms or the less variance of each term.  
Fig. A2b shows the covariance between models and observations. As can be seen in this figure, the mean value of covariance  
for the S components is larger than the M. So, the smaller correlation of S in comparison to that of M is attributed to the larger



280 variability of S (Fig. A2c). In other words, the better model performance (i.e., smaller E3 and MSE) for the M is not associated with the larger covariance of the M component. That is attributed to the less variance of the M than that of the S, see Fig. 3 and Fig. A2c.

In order to examine the effect of the CAMS products and lagged O<sub>3</sub> on the LSTM model, we exclude the lagged ozone from the predictors of the LSTM model, hereafter LSTM<sup>no\_lag</sup>. The R<sup>2</sup> of the LSTM<sup>no\_lag</sup> is shown in Fig. A3. Overall, the R<sup>2</sup> of the LSTM<sup>no\_lag</sup> is less than that of the LSTM. This suggests that the LSTM<sup>no\_lag</sup> may carry the risk of not including all important  
285 predictors (e.g., lagged ozone) in the model. This feature is more noticeable in the M term than the S term, i.e., the R<sup>2</sup> of the S component is less affected by removing the lagged O<sub>3</sub>. That reflects the CAMS products, which explain more of the S variability than that of the M term. In other words, most of the variability of the M term in the LSTM is explained by the lagged O<sub>3</sub> (not by the CAMS products). That could be a reason for the better performance (less MSE) of the M than the S. Figure A4a shows the MSE of the LSTM<sup>no\_lag</sup>. In this figure, the MSE of the datasets increases by two times with respect to  
290 that of the LSTM. The higher values of the MSE in the LSTM<sup>no\_lag</sup> are attributed to the removal of the lagged O<sub>3</sub> from the model. Although the R<sup>2</sup> of the LSTM<sup>no\_lag</sup> for the S is larger than that for the M term, the MSE of the S is higher than that of the M term. This is similar to the MSE of the LSTM, which is related to the higher variability of S than M. Similar to the LSTM, in LSTM<sup>no\_lag</sup>, the low values of MSE are seen for the S component of O<sub>3</sub> at stations 22 (Yazd), 20 (Hamedan), and 24 (Zanjan).

295 The skill score (SS) of the downscaled models O<sub>3</sub><sup>SD</sup> with respect to the O<sub>3</sub><sup>RA</sup> and O<sub>3</sub><sup>FC</sup> for all datasets are shown in Fig. 6. In panel (a) of this figure, the mean value of SS for three datasets, namely CAMSRA\_S, CAMSRA\_M, and CAMSFC\_M is larger than 0.9. This reflects that the downscaling procedure (LSTM) improves the accuracy of the results in the three mentioned datasets. The lower value of the SS for CAMSFC\_S can be attributed to the higher skill of the reference dataset, i.e., O<sub>3</sub><sup>FC</sup>, or the less accuracy of the LSTM model. The SS of the LSTM<sup>no\_lag</sup> for CAMSRA\_S shows the same high accuracy  
300 as that in the LSTM, whereas for other datasets the mean SS declines to 0.5 (see Fig. 6b).

## 5 Discussion

Analysis of the spectral components in this study reveals that the O<sub>3</sub> variability in both CAMS products possesses a nearly similar shape (although in different phases and amplitudes) as those in OBS. Results of the models' performances show a larger MSE for the S than that for the M in both CAMS. That arises from the larger variabilities of the S in comparison to the  
305 M (Hogrefe et al., 2000; Hogrefe et al., 2014; Kaffashzadeh 2018; Kaffashzadeh and Aliakbari Bidokhti, 2022). The results of error apportionment show the negligible contribution of the E2 to the MSE. E2 arises from the limited spatial resolutions of the CAMS in capturing short- and meso-scale phenomena that are attenuated (alleviated) by the SDS procedures. The MSE has mostly arisen from the E3, which emphasizes the lack of observed variability in the CAMS data. The E3 assessment shows less variability for both components of O<sub>3</sub><sup>SD</sup> than in O<sub>3</sub><sup>OBS</sup>. That could arise from random errors inherent in the OBS data due  
310 to sub-scale or non-resolvable processes in an observational network. The variability in the measured data might be generated



from the non-representatives' errors due to random effects caused by turbulence or sub-scale perturbations (Gandin, 1988; Steinacker et al., 2011). It is not straightforward to distinguish and exclude these errors in the measured data because of their chaotic and unsystematic behaviors. Adding the lagged  $O_3$  to the predictors of the downscaled model halves the E3 (and MSE). Less MSE of the M in comparison to that of the S attributes to not only the less variance of the M than the S but also the larger contribution of the lagged  $O_3$  in the M than that in the S (as shown in Sect. 4). The S component shows large associations with meteorological variables such as T2m, BLH, U10m, and V10m and pollutant species such as CO, NO, and  $NO_2$ . That is due to short-term  $O_3$  fluctuations associated with processes such as vertical mixing, local NO titration, wind speeds, solar flux, etc. The S component shows the large value of MSE for the stations located in Tehran, Shiraz, and Tabriz, which are known as the most populated cities (and so large emissions sources) in Iran. The largest MSE belongs to  $O_3$  at the stations over Tehran (see Fig. A4). That can be partly attributed to the complex topography and local (meso) scale flow (e.g., slope, mountain, and valley flow) over the city. The pollutant concentrations are highly affected by these factors, which are hardly captured by the global chemistry models (Fiore et al., 2003). The MSE of  $O_3$  over Tehran in the warm season is much higher than that in the cold season (see Fig. A5). That could arise from the uncertainty of  $O_3$  precursors in CAMS, as in summer, rising temperatures speed up the rate of many reactions and enhance biogenic VOC emissions (Sillman and Samson, 1995). The city of Tehran suffers from a high level of emitted  $NO_x$  from several sources, such as road traffic, industrial activities, the energy conversion sector, etc. (Hosseini and Shahbazi, 2016; Yousefian et al., 2020). The latest Tehran emission inventory indicates that the annual emissions of VOC and  $NO_x$  are approximately 91 and 103 thousand tons, respectively (Shahbazi et al., 2022). The contributions of vehicles to VOCs and  $NO_x$  emissions are estimated to be 79 % and 35.2 %, respectively. These values increase to 79.5 % and 37.2 %, respectively, in the summer. In addition to the aforementioned factors, what distinguishes Tehran from other cities is the difference between day and nighttime populations. During the day, traffic in Tehran reaches its highest level due to the arrival of private vehicles and passenger and cargo transportation vehicles from surrounding areas and cities. This issue has a significant impact on the city's traffic and the vehicle traffic on intercity routes leading to Tehran. Since Tehran is the political and economic capital of the country, this has resulted in the emergence of urban and industrial areas in the nearby areas of the city. For instance, Karaj city, with a population of over 1.6 million, is located 30 km west of Tehran and upstream of the prevailing wind direction. So, emitted ozone precursors in urban and industrial areas located around the city can transfer to Tehran (Shahbazi and Hosseini, 2020). The MSE distribution over Tehran is uneven; the northern part of the city shows a larger MSE than that over the southern part. That can be attributed to the uncertainty of the simulated CO species, as it is selected as a predictor at the stations located in the northern part. The CO concentration increases, moving from the south to the north of Tehran (Sharipour and Aliakbari Bidokhti, 2014).

The large MSE of  $O_3^{SD}$  for the cities of Shiraz and Tabriz is mostly associated with the geographical locations of the cities. Tabriz is the largest economic (industrialized) hub and metropolitan area in northwestern Iran. Numerous cars commuting and polluting industries such as thermal power plants and oil refineries in the west of the city are responsible for poor air quality over Tabriz. This city is surrounded by mountains and located in the vicinity of the eastern Mediterranean, a well-known region of tropopause folding activities that often increase the tropospheric ozone level and variability in summer (Tyrllis et al., 2014;



345 Zanis et al., 2014; Akritidis et al., 2016). Tabriz is often affected by cyclonic activities (Asakereh and Khojasteh, 2021) and  
summer circulations over the eastern Mediterranean region (Tyrlis et al., 2013). Although CAMSRA captures the long-range  
transport processes and atmospheric background in the troposphere, it shows a lower skill over the Mediterranean, in particular  
the eastern part, compared to other regions (Errera et al., 2021). Shiraz, as the capital of Fars province, is the largest city with  
more than 1.2 million inhabitants in the southwestern of Iran. This city has a high level of air pollution due to population  
350 growth, urbanization, and traffic-related emissions. The city is located in a valley between two mountain ranges with east-west  
orientations. The model representation of the terrain is considered to be an important key factor for achieving a good  
representation of the wind flow in complex terrain (Mughal et al., 2017). The low MSE values in the cities of Yazd, Hamedan,  
and Zanjan are associated with the station locations, which are less populated and affected by the emissions sources.  
To assess the sensitivity and robustness of the results to SD methods, the data are downscaled using another SD method,  
355 namely the multiple linear regression (MLR) model. In this model, the predictors and predictand were the same as the LSTM  
model. Figure A6b shows the MSE of  $O_3^{SD}$  with the MLR model. In similarity with the LSTM model (similar to the results in  
Sect. 4), the MSE for the S is larger than the M components downscaled with the MLR model. Although the mean value of  
the MSE of the downscaled data with the MLR is slightly less than that of the LSTM. That could arise from the larger  
correlation (and covariance) between downscaled datasets and OBS in the MLR model. Similar to the LSTM, the SS of the  
360 MLR is high for all downscaled datasets; the SS for the CAMSFC\_S datasets is less than other datasets (see Fig. A7a).

## 6 Conclusions

In this paper, the variability of  $O_3$  in two datasets, namely CMASRA and CAMSFC, was assessed against observations at 27  
urban stations distributed over Iran. To cope with the limited spatial resolutions of CAMS, the data were downscaled using an  
LSTM neural network. The most relevant peroxides were found by screening several meteorological variables and chemical  
365 species. We decomposed all datasets into three spectral components, i.e., short (S), medium (M), and long (L) terms. The S  
term consists of intraday and diurnal variations; the M term includes synoptic multiday fluctuations; and the other motions,  
i.e., seasonal, semi-seasonal, and trend, are carried in the L. We only assessed the S and M terms due to the availability of one-  
year data, i.e., 2020; the L component is primarily used to check the biases between model data and observations but should  
not be considered reliable with respect to trend analysis, etc. Since S and M components have zero-mean fluctuations, the bias  
370 term (distance between the time average of model data and observations) is zero, and the main focus of this study was to  
analyze the variability terms, e.g., variance and covariance. The results presented in this study reveal several key points:  
(1) Various variables were identified as potential predictors of ozone. The S term shows high associations with temperature,  
10 m wind components, and  $NO_x$ , while the M component shows higher associations with cloud cover and simulated ozone.  
In CAMSFC, boundary layer height appears to be the dominant meteorological driver of the S component. The  $R^2$  of the LSTM  
375 model for the M component is larger than that for the S term, despite a smaller number of predictors for M than for S. That  
might reflect that more predictors would not imply a better model.



(2) The SS of the downscaled CAMSFC\_S is lower than other datasets. This can be attributed to the higher skill of the reference dataset, i.e.,  $O_3^{FC}$ . The SS of the LSTM<sup>no\_lag</sup> for CAMSRA\_S shows the same high accuracy as LSTM, whereas for other datasets the mean SS declines to 0.5. The robustness of the results was confirmed using additional downscaling procedures, i.e., MLR.

(3) Both datasets, i.e., CAMSRA and CAMSFC, show less MSE for the M component than for the S term. That is mainly attributed to the low variability of M and is not related to the large covariance of this component. The MSE was mainly associated with unexplained model errors (E3), which could be caused by the CAMS deficiency in resolving the mesoscale phenomena such as local winds, NO titration, and their impact on  $O_3$  variability.

(4) In both datasets, the highest MSE belongs to  $O_3^{SD}$  at stations over Tehran in the warm season. That arises from the uncertainty of  $O_3$  precursors, e.g.,  $NO_x$ , in CAMS. This can be considered a starting point for improving the results of tropospheric ozone, in particular at urban sites.

**Code availability.** The Python 3.7 code of the methodology will be available in the Zenodo.

**Data availability.** Part of the observational data is accessible from the <http://airnow.tehran.ir/home/DataArchive.aspx> portal. CAMS reanalysis and forecast datasets were obtained through ECMWF's atmospheric data service (last access: April 2022).

**Author contribution:** N. K designed the research, acquired and processed all data, performed the statistical analysis, and composed the figures and manuscript. A. A. B. contributed to proofreading.

**Competing interests:** The authors declare no competing interests.

**Disclaimer:** Publisher's note: Copernicus Publications remains neutral with regard to jurisdictional claims in published maps and institutional affiliations.

**Acknowledgements.** This study has been supported by the National Vice-Presidency for Science and Technology Affairs of Iran for N. K. We thank the data providers of the Iran Environmental Protection Organization, Tehran Air Quality Control Company, and the ECMWF's climate data services. Appreciations is given to M. G. Schultz for his help in training N.K.

## References

Ahmed, K., Shahid, S., Haroon, S. B., Xiao-jun, W.: Multilayer perceptron neural network for downscaling rainfall in arid region: A case study of Baluchistan, Pakistan. *J Earth Syst Sci*, 124, 1325- 1341, <https://doi.org/10.1007/s12040-015-0602-9>, 2015.



- 405 Akritidis, D., Pozzer, A., Zanis, P., Tyrlis, E., Škerlak, B., Sprenger, M., and Lelieveld, J.: On the role of tropopause folds in  
sum- mertime tropospheric ozone over the eastern Mediterranean and the Middle East, *Atmos. Chem. Phys.*, 16, 14025–14039,  
<https://doi.org/10.5194/acp-16-14025-2016>, 2016.
- Asakereh, H. and Khojasteh, A.: Frequency of entrance Mediterranean Cyclones to Iran and Their Impact on Widespread  
precipitation, *Journal of Natural Environmental Hazards*, 10, 27, 159-176, [10.22111/jneh.2020.33171.1632](https://doi.org/10.22111/jneh.2020.33171.1632), 2021.
- 410 Basart, S., Benedictow, A., Bennouna, Y., Blechschmidt, A.-M., Chabrillat, S., Christophe, Y., Cuevas, E., Eskes, H. J.,  
Hansen, K. M., Jorba, O., Kapsomenakis, J., Langerock, B., Pay, T., Richter, A., Sudarchikova, N., Schulz, M., Wagner, A.,  
and Zerefos, C.: Upgrade verification note for the CAMS real-time global atmospheric composition service: Evaluation of the  
e-suite for the CAMS upgrade of July 2019, Copernicus Atmosphere Monitoring Service (CAMS) report, 118 pp.,  
[doi:10.24380/fcwq-yp50](https://doi.org/10.24380/fcwq-yp50), 2019.
- Beecham, S., Rashid, M., Chowdhury, R. K.: Statistical downscaling of multi-site daily rainfall in a South Australian catchment  
415 using a Generalized Linear Model, *Int J Climatol*, 34, 3654-3670, <https://doi.org/10.1002/joc.3933>, 2014.
- Bell, M. L., Peng, R. D., and Dominici, F.: The Exposure – Response Curve for Ozone and Risk of Mortality and the Adequacy  
of Current Ozone Regulations, *Environ Health Perspect*, 114, 4, 532–536, <https://doi.org/10.1289/ehp.8816>, 2006.
- Bidokhti, A. A., Shariepour, Z., and Sehatkashani, S.: Some resilient aspects of urban area to air pollution and climate change,  
case study: tehran, Iran, 23, 1994–2005, 2016.
- 420 Bloomer, B. J., Stehr, J. W., Piety, C. A., Salawitch, R. J., and Dickerson, R. R.: Observed relationships of ozone air pollution  
with temperature and emissions, *Geophys. Res. Lett.*, 36, 1–5, <https://doi.org/10.1029/2009GL037308>, 2009.
- Borhani, F., Shafiepour Motlagh, M., Stohl, A., Rashidi, Y., and Ehsani, A. H.: Tropospheric Ozone in Tehran, Iran, during  
the last 20 years, *Environ. Geochem. Health*, 4, <https://doi.org/10.1007/s10653-021-01117-4>, 2021.
- Cooper, O.R., Parrish, D.D., Ziemke, J., Balashov, N. V., Cupeiro, M., Galbally, I. E., Gilge, S., Horowitz, L., Jensen, N. R.,  
425 Lamarque, J.-F., Naik, V., Oltmans, S. I., Schwab, J., Shindell, D. T., Thompson, A. M., Thouret, V., Wang, Y., and Zbinden,  
R. M.: Global distribution and trends of tropospheric ozone: An observation-based review, *Elementa Sci. Anthropocene*, 2,  
000029, [doi:10.12952/journal.elementa.000029](https://doi.org/10.12952/journal.elementa.000029), 2014.
- Crutzen, P. J.: Photochemical reactions initiated by and influencing ozone in unpolluted tropospheric air, *Tellus*, 26, 47–57,  
<https://doi.org/10.3402/tellusa.v26i1-2.9736>, 1974.
- 430 Errera, Q., Bennouna, Y., Schulz, M., Eskes, H. J., Basart, S., Benedictow, A., Blechschmidt, A.-M., Chabrillat, S., Clark, H.,  
Cuevas, E., Flentje, H., Hansen, K. M., Im, U., Kapsomenakis, J., Langerock, B., Petersen, K., Richter, A., Sudarchikova, N.,  
Thouret, V., Wagner, A., Wang, Y., Warneke, T., and Zerefos, C.: Validation report of the CAMS global Reanalysis of aerosols  
and reactive gases, years 2003-2020, Copernicus Atmosphere Monitoring Service (CAMS) report,  
[CAMS84\\_2018SC3\\_D5.1.1-2020.pdf](https://doi.org/10.24380/8gf9-k005), [doi:10.24380/8gf9-k005](https://doi.org/10.24380/8gf9-k005), 206 pp., June 2021.
- 435 Eskes, H. J., Basart, S., Benedictow, A., Bennouna, Y., Blechschmidt, A.-M., Errera, Q., Hansen, K. M., Kapsomenakis, J.,  
Langerock, B., Richter, A., Sudarchikova, N., Schulz, M., and Zerefos, C.: Upgrade verification note for the CAMS near-real



- time global atmospheric composition service: Evaluation of the e-suite for the CAMS 47R3 upgrade of 12 October 2021, Copernicus Atmosphere Monitoring Service (CAMS) report, doi:10.24380/hfvp-fq98, 91 pp., October 2021.
- 440 Eskridge, R. E., Ku, J. Y., Rao, S. T., Porter, P. S., and Zurbenko, I. G.: Separating Different Scales of Motion in Time Series of Meteorological Variables, *Bulletin of the American Meteorological Society*, 78, 7, 1473–1484, [https://doi.org/10.1175/1520-0477\(1997\)078<1473:SDSOMI>2.0.CO;2](https://doi.org/10.1175/1520-0477(1997)078<1473:SDSOMI>2.0.CO;2), 1997.
- Faridi, S., Shamsipour, M., Krzyzanowski, M., Künzli, N., Amini, H., Azimi, F., Malkawi, M., Momeniha, F., Gholampour, A., Hassanvand, M. S., and Naddafi, K.: Long-term trends and health impact of PM<sub>2.5</sub> and O<sub>3</sub> in Tehran, Iran, 2006–2015, *Environ. Int.*, 114, 37–49, <https://doi.org/10.1016/j.envint.2018.02.026>, 2018.
- 445 Fiore, A. M., Jacob, D. J., Mathur, R., and Martin, R. V.: Application of empirical orthogonal functions to evaluate ozone simulations with regional and global models, *J. Geophys. Res.*, 108, 4431, doi:10.1029/2002JD003151, 2003.
- Flemming, J., Huijnen, V., Arteta, J., Bechtold, P., Beljaars, A., Blechschmidt, A.-M., Diamantakis, M., Engelen, R. J., Gaudel, A., Inness, A., Jones, L., Josse, B., Katragkou, E., Marecal, V., Peuch, V.-H., Richter, A., Schultz, M. G., Stein, O., and Tsikerdekis, A.: Tropospheric chemistry in the Integrated Forecasting System of ECMWF, *Geosci. Model Dev.*, 8, 975–  
450 1003, <https://doi.org/10.5194/gmd-8-975-2015>, 2015.
- Fowler, D., Pilegaard, K., Sutton, M. A., Ambus, P., Raivonen, M., Duyzer, J., Simpson, D., Fagerli, H., Fuzzi, S., Schjoerring, J. K., Granier, C., Neftel, A., Isaksen, I. S. A., Laj, P., Maione, M., Monks, P. S., Burkhardt, J., Daemmgen, U., Neiryneck, J., Per-  
sonne, E., Wichink-Kruit, R., Butterbach-Bahl, K., Flechard, C., Tuovinen, J. P., Coyle, M., Gerosa, G., Loubet, B., Altimir, N., Gruenhage, L., Ammann, C., Cieslik, S., Paoletti, E., Mikkelsen, T. N., Ro-Poulsen, H., Cellier, P., Cape, J. N.,  
455 Horvath, L., Loreto, F., Niinemets, U., Palmer, P. I., Rinne, J., Misztal, P., Nemitz, E., Nilsson, D., Pryor, S., Gallagher, M. W., Vesala, T., Skiba, U., Brüeggemann, N., Zechmeister-Boltenstern, S., Williams, J., O’Dowd, C., Facchini, M. C., de Leeuw, G., Floss-  
man, A., Chaumerliac, N., and Erismann, J. W.: Atmospheric composition change: Ecosystems-Atmosphere interactions, *Atmos. Environ.*, 43, 5193–5267, doi:10.1016/j.atmosenv.2009.07.068, 2009.
- Gandin, L. S.: Complex Quality Control of Meteorological Observations, *Monthly Weather Review*, 116(5), 1137–1156, 460  
doi:10.1175/1520-0493(1988)116<1137:CQCOMO>2.0.CO;2, 1988.
- Gerharz, L., Gräler, B., and Pebesma, E.: Measurement artefacts and inhomogeneity detection, technical report, Uni. Münster, Germany, under subcontract of ETC/ACM Consortium institute RIVM, ETC/ACM, 54 pp., 2011.
- Granier, C., Bessagnet, B., Bond, T., D’Angiola, A., Denier van der Gon, H., Frost, G. J., Heil, A., Kaiser, J. W., Kinne, S., Klimont, Z., Kloster, S., Lamarque, J.-F., Liousse, C., Masui, T., Meleux, F., Mieville, A., Ohara, R., Raut, J.-C., Riahi, K.,  
465 Schultz, M. G., Smith, S. G., Thompson, A., van Aardenne, J., van der Werf, G. R., and van Vuuren, D. P.: Evolution of anthropogenic and biomass burning emissions of air pollutants at global and regional scales during the 1980–2010 period, *Climatic Change*, 109, 163–190, <https://doi.org/10.1007/s10584-011-0154-1>, 2011.
- Granier, C., Darras, S., Denier van der Gon, H. A. C., Doubalova, J., Elguindi, N., Galle, B., Gauss, M., Guevara, M., Jalkanen, J.-P., Kuenen, J., Liousse, C., Quack, B., Simpson, D., and Sindelarova, K.: The Copernicus Atmosphere Monitoring Service



- 470 global and regional emissions (April 2019 version), Copernicus Atmosphere Monitoring Service (CAMS) report, 54 pp.,  
<https://doi.org/10.24380/d0bn-kx16>, 2019.
- Guenther, A., Karl, T., Harley, P., Wiedinmyer, C., Palmer, P. I., and Geron, C.: Estimates of global terrestrial isoprene emissions using MEGAN (Model of Emissions of Gases and Aerosols from Nature), *Atmos. Chem. Phys.*, 6, 3181–3210, <https://doi.org/10.5194/acp-6-3181-2006>, 2006.
- 475 Hadei, M., Hopke, P. K., Nazari, S. S. H., Yarahmadi, M., Shamsavani, A., and Alipour, M. R.: Estimation of mortality and hospital admissions attributed to criteria air pollutants in Tehran metropolis, Iran (2013–2016), *Aerosol and Air Quality Research*, 17, 2474–2481, <https://doi.org/10.4209/aaqr.2017.04.0128>, 2017.
- Haiden, T., Janousek, M., Vitart, F., Ferranti, L., and Prates, F.: Evaluation of ECMWF forecasts, including the 2019 upgrade, ECMWF Technical Memoranda No. 853, 54 pp., 2019.
- 480 Hochreiter, S. and Schmidhuber, J.: Long Short-Term Memory, *Neural Computation*, 9, 8, 1735–1780, 1997.
- Hogrefe, C., Rao, S. T., Zurbenko, I. G., and Porter, P. S.: Interpreting the Information in Ozone Observations and Model Predictions Relevant to Regulatory Policies in the Eastern United States, *Bulletin of the American Meteorological Society*, 8, 9, 2083–2106, <http://www.jstor.org/stable/26215189>, 2000.
- Hogrefe, C., Roselle, S., Mathur, R., Rao, S. T., and Galmarini, S.: Space-time analysis of the Air Quality Model Evaluation International Initiative (AQMEII) Phase 1 air quality simulations, *J. Air Waste Manag. Assoc.*, 64, 388–405, <https://doi.org/10.1080/10962247.2013.811127>, 2014.
- 485 Hosseini, V. and Shahbazi, H.: Urban Air Pollution in Iran. *Iranian Studies*, 49, 6, 1029–1046, doi:10.1080/00210862.2016.1241587, 2016.
- Huijnen, V., Williams, J., van Weele, M., van Noije, T., Krol, M., Dentener, F., Segers, A., Houweling, S., Peters, W., de Laat, J., Boersma, F., Bergamaschi, P., van Velthoven, P., Le Sager, P., Eskes, H., Alkemade, F., Scheele, R., Nédélec, P., and Pätz, H.-W.: The global chemistry transport model TM5: description and evaluation of the tropospheric chemistry version 3.0, *Geosci. Model Dev.*, 3, 445–473, <https://doi.org/10.5194/gmd-3-445-2010>, 2010.
- Huijnen, V., Miyazaki, K., Flemming, J., Inness, A., Sekiya, T., and G. Schultz, M.: An intercomparison of tropospheric ozone reanalysis products from CAMS, CAMS interim, TCR-1, and TCR-2, *Geosci. Model Dev.*, 13, 1513–1544, <https://doi.org/10.5194/gmd-13-1513-2020>, 2020.
- 495 Inness, A., Ades, M., Agustí-Panareda, A., Barr, J., Benedictow, A., Blechschmidt, A. M., Jose Dominguez, J., Engelen, R., Eskes, H., Flemming, J., Huijnen, V., Jones, L., Kipling, Z., Massart, S., Parrington, M., Peuch, V. H., Razinger, M., Remy, S., Schulz, M., and Suttie, M.: The CAMS reanalysis of atmospheric composition, *Atmos. Chem. Phys.*, 19, 3515–3556, <https://doi.org/10.5194/acp-19-3515-2019>, 2019.
- 500 Jafari Hombari, F. and Pazhoh, F.: Synoptic analysis of the most durable pollution and clean waves during 2009 – 2019 in Tehran City (capital of Iran), *Nat. Hazards*, 110, 1247–1272, <https://doi.org/10.1007/s11069-021-04990-5>, 2022.





- Kaffashzadeh, N.: A Statistical Analysis of Surface Ozone Variability Over the Mediterranean Region During Summer, Ph.D. thesis, Rheinische Friedrich-Wilhelms-Universität Bonn, Germany, <https://nbn-resolving.org/urn:nbn:de:hbz:5n-52000>, 130 pp., 2018.
- 505 Kaffashzadeh, N. and Aliakbari Bidokhti, A. A.: Temporal variability analysis of measured surface ozone at the Geophysics Institute Station of the University of Tehran, *Journal of the Earth and Space Physics*, 48, 3, 673-691. doi: 10.22059/jesphys.2022.329346.1007355, 2022.
- Kaiser, J. W., Heil, A., Andreae, M. O., Benedetti, A., Chubarova, N., Jones, L., Morcrette, J.-J., Razinger, M., Schultz, M. G., Suttie, M., and van der Werf, G. R.: Biomass burning emissions estimated with a global fire assimilation system based on observed fire radiative power, *Biogeosciences*, 9, 527–554, <https://doi.org/10.5194/bg-9-527-2012>, 2012.
- 510 Kang, D., Hogrefe, C., Foley, K. L., Napelenok, S. L., Mathur, R., and Rao, S. T.: Application of the Kolmogorov Zurbenko filter and the decoupled direct 3D method for the dynamic evaluation of a regional air quality model, *Atmos. Environ.*, 80, 58–69, <https://doi.org/10.1016/j.atmosenv.2013.04.046>, 2013.
- Khansalari, S., Ghobadi, N., Aliakbari Bidokhti, A., and Fazel Rastgar, F.: Statistical classification of synoptic weather patterns associated with Tehran air pollution, *Journal of Air Pollution and Health*, 5, 43–62, <https://doi.org/10.18502/japh.v5i1.2858>, 2020.
- 515 Kilsby, C. G., Jones, P., Burton, A., Ford, A., Fowler, H. J., Harpham, C., James, P., Smith, A., and Wilby, R.: A daily weather generator for use in climate change studies, *Environmental Modelling & Software*, 22, 12, 1705–1719, <https://doi.org/10.1016/j.envsoft.2007.02.005>, 2007.
- 520 Lashkari, H., Keikhosravi, G., and Karimian, N.: Investigating Patterns of Severe Air Pollution in the Lower Tropospheric Layer of Tehran Metropolitan, *J. Geogr. Environ. Hazards*, 9, 1–20, <https://doi.org/10.22067/geo.v9i3.87260>, 2020.
- Lelieveld, J., Hoor, P., Jöckel, P., Pozzer, A., Hadjinicolaou, P., Cammas, J. P., and Beirle, S.: Severe ozone air pollution in the Persian Gulf region, *Atmos. Chem. Phys.*, 9, 1393–1406, <https://doi.org/10.5194/acp-9-1393-2009>, 2009.
- 525 Li, K., Jacob, D. J., Shen, L., Lu, X., Smedt, I. De, and Liao, H.: Increases in surface ozone pollution in China from 2013 to 2019: anthropogenic and meteorological influences, *Atmos. Chem. Phys.*, 20, 11423–11433, <https://doi.org/10.5194/acp-20-11423-2020>, 2020.
- Loneck, B., and Zurbenko, I.: Theoretical and Practical Limits of Kolmogorov-Zurbenko Periodograms with DiRienzo-Zurbenko Algorithm Smoothing in the Spectral Analysis of Time Series Data Barry, arXiv [preprint], arXiv:2007.03031v1, 28 pp., 2020.
- 530 Malley, C. S., Heal, M. R., Mills, G., and Braban, C. F.: Trends and drivers of ozone human health and vegetation impact metrics from UK EMEP supersite measurements (1990 – 2013), *Atmos. Chem. Phys.*, 15, 4025–4042, <https://doi.org/10.5194/acp-15-4025-2015>, 2015.
- Michou, M., Laville, P., Serça, D., Fotiadi, A., Bouchou, P., and Peuch, V.-H.: Measured and modeled dry deposition velocities over the ESCOMPTE area, *Atmos. Res.*, 74, 89–116, 2004.



- 535 Mills, G., Hayes, F., Simpson, D., Emberson, L., Norris, D., Har- mens, H., and Büker, P.: Evidence of widespread effects of ozone on crops and (semi-)natural vegetation in Europe (1990–2006) in relation to AOT40- and flux-based risk maps, *Global Change. Biol.*, 17, 592–613, <https://doi.org/10.1111/j.1365-2486.2010.02217.x>, 2011.
- Monks, P. S., Archibald, A. T., Colette, A., Cooper, O., Coyle, M., Derwent, R., Fowler, D., Granier, C., Law, K. S., Mills, G. E., Stevenson, D. S., Tarasova, O., Thouret, V., von Schneidemesser, E., Sommariva, R., Wild, O., and Williams, M. L.:
- 540 Tropospheric ozone and its precursors from the urban to the global scale from air quality to short-lived climate forcer, *Atmos. Chem. Phys.*, 15, 8889–8973, <https://doi.org/10.5194/acp-15-8889-2015>, 2015.
- Mughal, M. O., Lynch, M., Yu, F., McGann, B., Jeanneret, F., and Sutton, J.: Wind modelling, validation and sensitivity study using Weather Research and Forecasting model in complex terrain, *Environmental Modelling & Software*, 90, 107–125, <https://doi.org/10.1016/j.envsoft.2017.01.009>, 2017.
- 545 Murphy, A. H.: Skill Scores Based on the Mean Square Error and Their Relationships to the Correlation Coefficient, *Monthly Weather Review*, 116, 2417–2424, [https://doi.org/10.1175/1520-0493\(1988\)116<2417:SSBOTM>2.0.CO;2](https://doi.org/10.1175/1520-0493(1988)116<2417:SSBOTM>2.0.CO;2), 1988.
- Murazaki, K. and Hess, P.: How does climate change contribute to surface ozone change over the United States?, *J. Geophys. Res.*, 111, 1–16, <https://doi.org/10.1029/2005JD005873>, 2006.
- Park, S., Son, S. W., Jung, M. Il, Park, J., and Park, S. S.: Evaluation of tropospheric ozone reanalyses with independent
- 550 ozonesonde observations in East Asia, *Geosci. Lett.*, 7, <https://doi.org/10.1186/s40562-020-00161-9>, 2020.
- Rao, S. T., Zurbenko, I. G., Neagu, R., Porter, P. S., Ku, J. Y., and Henry, R. F.: Space and Time Scales in Ambient Ozone Data, *Bulletin of the American Meteorological Society*, 78, 10, 2153–2166, [https://doi.org/10.1175/1520-0477\(1997\)078<2153:SATSIA>2.0.CO;2](https://doi.org/10.1175/1520-0477(1997)078<2153:SATSIA>2.0.CO;2), 1997.
- Sachindra, D. A., Huang, F., Barton, A. F., and Perera, B. J. C.: Least square support vector and multi-linear regression for
- 555 statistically downscaling general circulation model outputs to catchment streamflows. *Int J Climatol*, 33, 1087–1106, <https://doi.org/10.1002/joc.3493>, 2013.
- Sachindra, D.A., Ahmed, K., Mamunur Rashid, Md., Shahid, S., and Perera, B. J. C.: Statistical downscaling of precipitation using machine learning techniques, *Atmospheric Research*, 212, 240–258, <https://doi.org/10.1016/j.atmosres.2018.05.022>, 2018.
- 560 Schulz, M., Errera, Q., Ramonet, M., Sudarchikova, N., Eskes, H. J., Basart, S., Benedictow, A., Bennouna, Y., Blechschmidt, A.-M., Chabrillat, S., Christophe, Y., Cuevas, E. El-Yazidi, A., Flentje, H., Fritzsche, P., Hansen, K. M., Im, U., Kapsomenakis, J., Langerock, B., Richter, A., Thouret, V., Wagner, A., Warneke, T., and Zerefos, C.: Validation report of the CAMS near-real-time global atmospheric composition service: Period December 2020 – February 2021, Copernicus Atmosphere Monitoring Service (CAMS) report, CAMS84\_2018SC3\_D1.1.1\_DJF2021.pdf, doi:10.24380/ f540-kb09, 190
- 565 pp., June 2021.
- Sebbar, B.e., Khabba, S., Merlin, O., Simonneaux, V., Hachimi, C. E., Kharrou M. H., and Chehbouni, A.: Machine-Learning-Based Downscaling of Hourly ERA5-Land Air Temperature over Mountainous Regions, *Atmosphere*, 14, 4, 610, <https://doi.org/10.3390/atmos14040610>, 2023.



- 570 Semenov, M. A. and Stratonovitch, P.: Use of multi-model ensembles from global climate models for assessment of climate change impacts, *Climate Research*, 41, 1, 1–14, <http://www.jstor.org/stable/24870469>, 2010.
- Seo, J., Youn, D., Kim, J. Y., and Lee, H.: Extensive spatiotemporal analyses of surface ozone and related meteorological variables in South Korea for the period 1999–2010, *Atmos. Chem. Phys.*, 14, 6395–6415, <https://doi.org/10.5194/acp-14-6395-2014>, 2014.
- 575 Shahbazi, H. and Hosseini V.: Impact of mobile source emission inventory adjustment on air pollution photochemical model performance, *Urban Climate*, 32, <https://doi.org/10.1016/j.uclim.2020.100618>, 2020.
- Shahbazi, H., Mostafazade Abolmaali, A., Alizadeh, H., Salavati, H., Zokaei, H., Zandavi, R., Torbatian, S., Yazgi, D., and Hosseini, V.: An emission inventory update for Tehran: The difference between air pollution and greenhouse gas source contributions, *Atmospheric Research*, 275, 106240, <https://doi.org/10.1016/j.atmosres.2022.106240>, 2022.
- 580 Sharipour, Z. and Aliakbari Bidokhti, A. A.: Investigation of spatial and temporal distributions of air pollutants over Tehran in cold months of 2011–2013, *Journal of Environmental Science and Technology*, 16, 1, 149–166, [https://jest.srbiau.ac.ir/article\\_8112.html?lang=en](https://jest.srbiau.ac.ir/article_8112.html?lang=en), 2014.
- Sillman, S. and Samson, P. J.: Impact of temperature on oxidant photochemistry in urban, polluted rural and remote environments, *J. Geophys. Res.*, 100, 11497–11508, <https://doi.org/10.1029/94JD02146>, 1995.
- 585 Sindelarova, K., Granier, C., Bouarar, I., Guenther, A., Tilmes, S., Stavrou, T., Müller, J.-F., Kuhn, U., Stefani, P., and Knorr, W.: Global data set of biogenic VOC emissions calculated by the MEGAN model over the last 30 years, *Atmos. Chem. Phys.*, 14, 9317–9341, <https://doi.org/10.5194/acp-14-9317-2014>, 2014.
- Sindelarova, K., Markova, J., Simpson, D., Huszar, P., Karlicky, J., Darras, S., and Granier, C.: High-resolution biogenic global emission inventory for the time period 2000 – 2019 for air quality modelling, *Earth Syst. Sci. Data*, 14, 251–270, <https://doi.org/10.5194/essd-14-251-2022>, 2022.
- 590 Solazzo, E. and Galmarini, S.: Error apportionment for atmospheric chemistry-transport models – a new approach to model evaluation, *Atmos. Chem. Phys.*, 16, 6263–6283, <https://doi.org/10.5194/acp-16-6263-2016>, 2016.
- Stein, O., Schultz, M. G., Bouarar, I., Clark, H., Huijnen, V., Gaudel, A., George, M., and Clerbaux, C.: On the wintertime low bias of Northern Hemisphere carbon monoxide found in global model simulations, *Atmos. Chem. Phys.*, 14, 9295–9316, <https://doi.org/10.5194/acp-14-9295-2014>, 2014.
- 595 Steinacker, R., Mayer, D., and Steiner, A.: Data Quality Control Based on Self-Consistency, *Monthly Weather Review*, 139, 12, 3974–3991, doi:10.1175/MWR-D-10-05024.1, 2011.
- Stevenson, D. S., Dentener, F. J., Schultz, M. G., Ellingsen, K., van Noije, T. P. C., Wild, O., Zeng, G., Amann, M., Atherton, C. S., Bell, N., Bergmann, D. J., Bey, I., Butler, T., Cofala, J., Collins, W. J., Derwent, R. G., Doherty, R. M., Drevet, J., Eskes, H. J., Fiore, A. M., Gauss, M., Hauglustaine, D. A., Horowitz, L. W., Isaksen, I. S. A., Krol, M. C., Lamarque, J. F., Lawrence, 600 M. G., Montanaro, V., Müller, J. F., Pitari, G., Prather, M. J., Pyle, J. A., Rast, S., Rodriguez, J. M., Sanderson, M. G., Savage, N. H., Shindell, D. T., Strahan, S. E., Sudo, K., and Szopa, S.: Multimodel ensemble simulations of present-day and near-future tropospheric ozone, *J. Geophys. Res. Atmos.*, 111, <https://doi.org/10.1029/2005JD006338>, 2006.



- Sudarchikova, N., Schulz, M., Errera, Q., Ramonet, M., Eskes, H. J., Basart, S., Benedictow, A., Bennouna, Y., Blechschmidt, A.-M., Chabrillat, S., Christophe, Y., Cuevas, E., El-Yazidi, A., Flentje, H., Fritzsche, P., Hansen, K. M., Im, U.,  
605 Kapsomenakis, J., Langerock, B., Richter, A., Thouret, V., Wagner, A., Warneke, T., and Zerefos, C.: Validation report of the CAMS near-real-time global atmospheric composition service: Period September - November 2020, Copernicus Atmosphere Monitoring Service (CAMS) report, CAMS84\_2018SC3\_D1.1.1\_SON2020.pdf, doi: 10.24380/rysv-7371, 159 pp., March 2021.
- Taylor, J. R. and Loescher, H. L.: Automated quality control methods for sensor data: a novel observatory approach,  
610 Biogeosciences, 10, 4957–4971, <https://doi.org/10.5194/bg-10-4957-2013>, 2013.
- Tripathi, S., Srinivas, V. V., and Nanjundiah, R. S.: Downscaling of precipitation for climate change scenarios: a support vector machine approach. J Hydrol, 330, 621-640, <https://doi.org/10.1016/j.jhydrol.2006.04.030>, 2006.
- Tyrlis, E., Lelieveld, J., and Steil, B.: The summer circulation over the eastern Mediterranean and the Middle East: influence of the South Asian monsoon, Climate Dynamics, 40, 1103–1123, <https://doi.org/10.1007/s00382-012-1528-4>, 2013.
- 615 Tyrlis, E., Škerlak, B., Sprenger, M., Wernli, H., Zittis, G., and Lelieveld, J.: On the linkage between the Asian summer monsoon and tropopause fold activity over the eastern Mediterranean and the Middle East, J. Geophys. Res.-Atmos., 119, 3202–3221, 2014.
- Wagner, A., Bennouna, Y., Blechschmidt, A., Brasseur, G., Chabrillat, S., Christophe, Y., Errera, Q., Eskes, H., Flemming, J., Hansen, K. M., Inness, A., Kapsomenakis, J., Langerock, B., Richter, A., Sudarchikova, N., Thouret, V., and Zerefos, C.:  
620 Comprehensive evaluation of the Copernicus Atmosphere Monitoring Service ( CAMS ) reanalysis against independent observations : Reactive gases, Elem Sci Anth, 9, <https://doi.org/10.1525/elementa.2020.00171>, 2021.
- Wang, Y., Ma, Y., Eskes, H., Inness, A., Flemming, J., and Brasseur, G. P.: Evaluation of the CAMS global atmospheric trace gas reanalysis 2003 – 2016 using aircraft campaign observations, Atmos. Chem. Phys., 20, 4493–4521, <https://doi.org/10.5194/acp-20-4493-2020>, 2020.
- 625 Wilby, R. L. and Wigley, T. M. L.: Downscaling general circulation model output: A review of methods and limitations. Prog Phys Geog, 21, 530-548, doi:10.1177/030913339702100403, 1997.
- Wilby, R. L., Charles, S. P., Zorita, E., Timbal, B., Whetton, P., and Mearns, L. O.: Guidelines for use of climate scenarios developed from statistical downscaling methods, supporting material to the IPCC, 3–21. Available at [https://www.ipcc-data.org/guidelines/dgm\\_NO2\\_v1\\_09\\_2004.pdf](https://www.ipcc-data.org/guidelines/dgm_NO2_v1_09_2004.pdf), , last access 1 November 2023, 2004.
- 630 Wilby, R. L. and Dawson, C. W.: The Statistical DownScaling Model: insights from one decade of application, Int. J. Climatol., 33, 1707-1719. <https://doi.org/10.1002/joc.3544>, 2013.
- Wilks, D. S.: Multisite downscaling of daily precipitation with a stochastic weather generator, Climate Research, 11, 125–136, <http://www.jstor.org/stable/24865983>, 1999.



- 635 Wilks, D. S.: Statistical Methods in the Atmospheric Sciences, international Geophysics Series, 91, 649 pp., second edition, 2006.
- Yang, W. and Zurbenko, I.: Kolmogorov – Zurbenko filters, WIREs Comp Stat, 2: 340-351. <https://doi.org/10.1002/wics.71>, 2010.
- 640 Yousefian, F., Faridi, S., Azimi, F., Aghaei, M., Shamsipour, M., Yaghmaeian, K., and Hassanvand, M. S.: Temporal variations of ambient air pollutants and meteorological influences on their concentrations in Tehran during 2012–2017, Sci. Rep., 10, 1–11, <https://doi.org/10.1038/s41598-019-56578-6>, 2020.
- Zahumenský, I.: Guidelines on Quality Control Procedures for Data from Automatic Weather Stations Guidelines on Quality Control Procedures for Data from Automatic Weather Stations, World Meteorological Organization, 10 pp., 2004.
- 645 Zanis, P., Hadjinicolaou, P., Pozzer, A., Tyrllis, E., Dafka, S., Mihalopoulos, N., and Lelieveld, J.: Summertime free-tropospheric ozone pool over the eastern Mediterranean/middle east, Atmos. Chem. Phys., 14, 115–132, <https://doi.org/10.5194/acp-14-115-2014>, 2014.
- Zohdirad, H., Montazeri Namin, M., Ashrafi, K., Aksoyoglu, S., and Prévôt, A. S. H.: Temporal variations, regional contribution, and cluster analyses of ozone and NO<sub>x</sub> in a middle eastern megacity during summertime over 2017–2019, Environ. Sci. Pollut. Res., 29, 16233–16249, <https://doi.org/10.1007/s11356-021-14923-1>, 2022.
- 650 Zurbenko, I., Porter, P. S., Gui, R., Rao, S. T., Ku, J. Y., & Eskridge, R. E.: Detecting discontinuities in time series of upper-air data: development and demonstration of an adaptive filter technique, Journal of Climate, 9, 12, 3548-3560, [https://doi.org/10.1175/1520-0442\(1996\)009<3548:DDITSO>2.0.CO;2](https://doi.org/10.1175/1520-0442(1996)009<3548:DDITSO>2.0.CO;2), 1996.

655

660

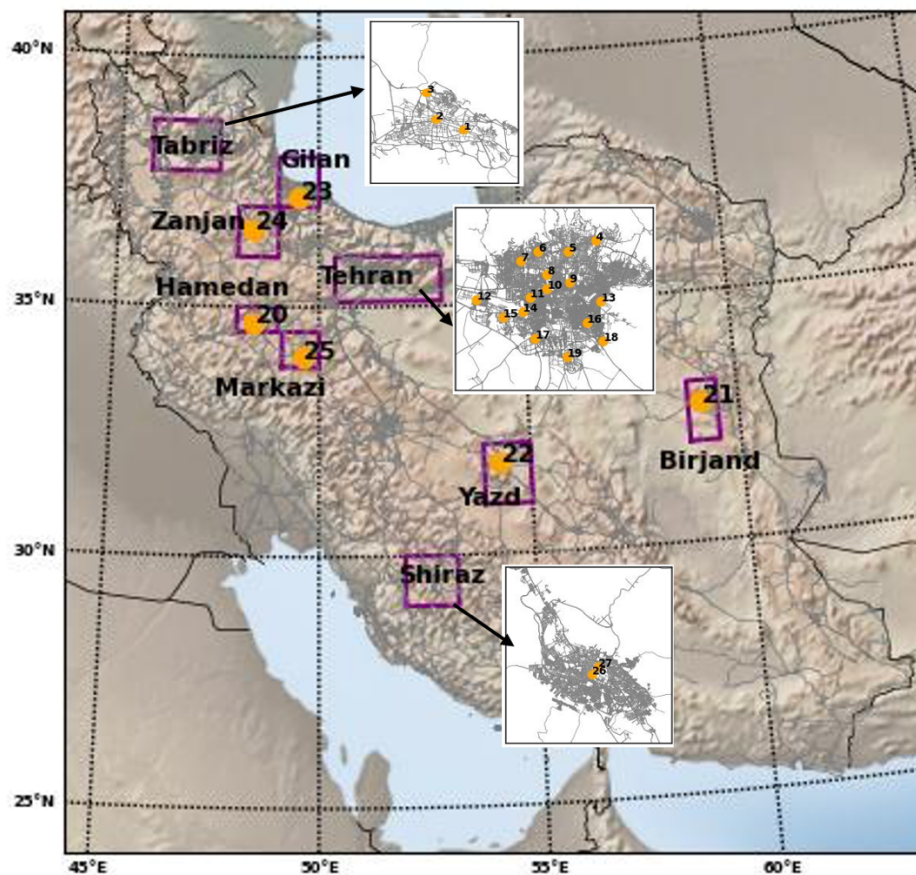
665



670

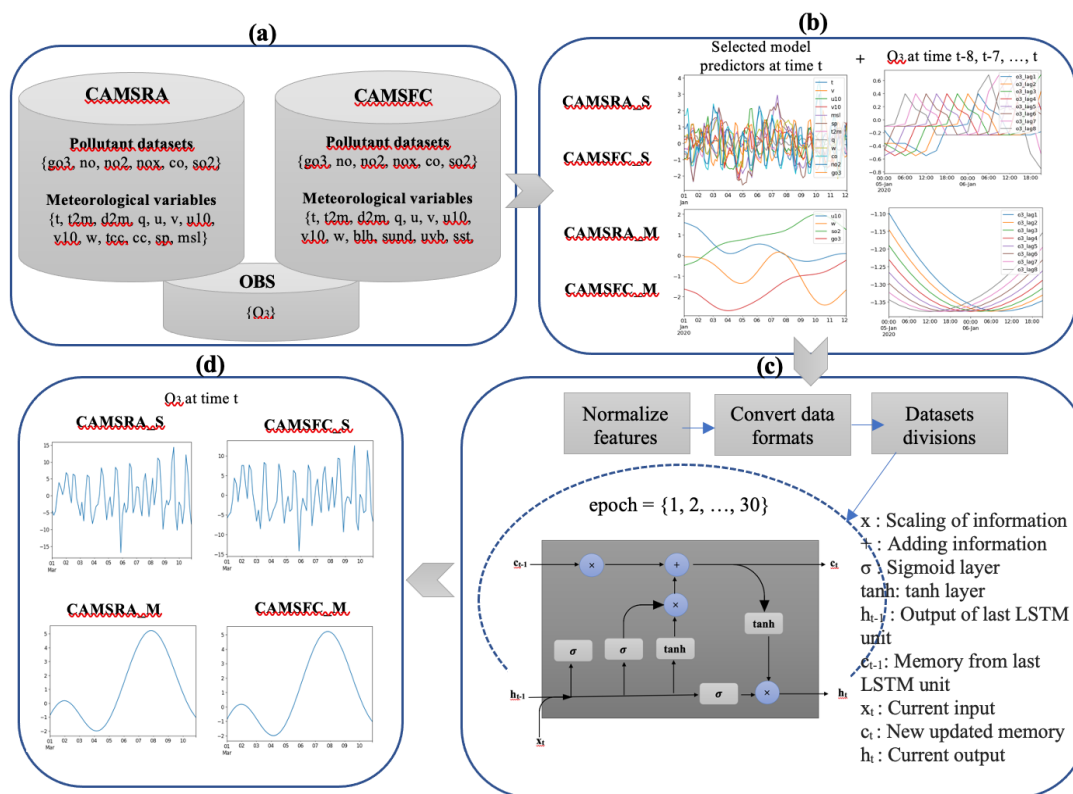
**Table 1. An overview of some similarities and differences between the CAMSRA and CAMSFC datasets used in this study**

<b>Name (references)</b>	<b>CAMSRA (Innes et al., 2019)</b>	<b>CAMSFC (Basart et al., 2019; Haiden et al., 2019; Sudarchikova et al., 2021)</b>
Temporal coverage	2003 to 2021	2015 to present
Assimilation system	IFS Cycle 42r1 4D-Var	IFS Cycle 46r1 (implemented on 9 July 2019) IFS Cycle 47r1 (implemented in 6 October 2020)
Horizontal resolution	0.75°x0.75° (T255)	0.4°x0.4° (T511)
Vertical resolution	L60 Up to 0.1 hPa	L137 up to 0.01 hPa
Temporal resolution (output frequency)	3 hourly	1 hourly (single level), 3 hourly (multi-level)
Anthropogenic emissions	MACCity	CAMS_GLOB_ANT v2.1 (cy46r1) CAMS_GLOB_ANT v4.2 (cy47r1)
Biomass burning emissions	GFASv1.2	GFASv1.2 (cy46r1) GFASv1.4 (cy47r1)
Biogenic emissions	MEGAN	CAMS_GLOB_BIO v1.1
Chemistry modules	modified CB05	modified CB05 with a few upgrades such as dry depositions velocity, coupling with aerosol scheme, etc.
Input meteorological observations	As in ERA5	As in ERA5



675

Figure 1. Geographical location and distribution of the measured air quality stations used in this study. The purple box areas correspond to the locations of the cities. Here the stations are represented with a number, details on the name and geographical coordinates of the stations are given in Table A1. The arrows refer to the stations, which are overlaid on the cities' maps of Tabriz, Tehran, and Shiraz (Fars).



680 **Figure 2.** A schematic of the downscaling processes: (a) input data retrieval, (b) decomposition and prescreening, (c) LSTM modeling, and (d) downscaled datasets.

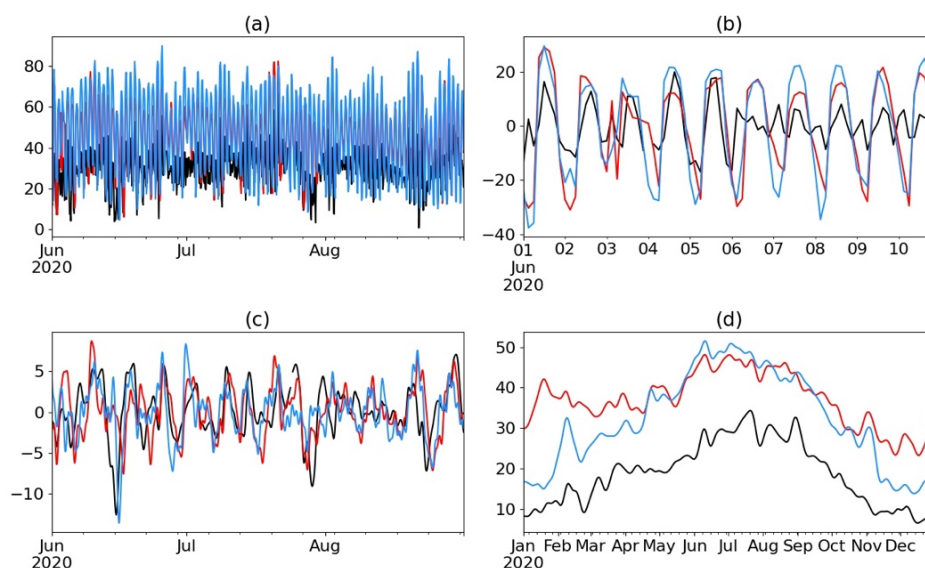


**Figure 3.** Different spectral components, i.e., (a) original time series, (b) short (S), (c) medium (M), and (d) long term (L) of  $O_3^{OBS}$  (black),  $O_3^{RA}$  (red), and  $O_3^{FC}$  (blue) at station 1. The vertical axis in all panels shows the ozone mixing ratio in  $nmol\ mol^{-1}$ .





685

**Table 2. The most important explanatory variables of the CAMSRA at each station**

Stations' number	S	M
1	T, V, U10m, V10m, MSLP, SP, T2m, SH, W, CO, NO <sub>2</sub> , O <sub>3</sub> <sup>RA</sup>	U10m, W, CO, O <sub>3</sub> <sup>RA</sup>
2	MSLP, SP, T2m, SH, W, NO <sub>2</sub> , O <sub>3</sub> <sup>RA</sup>	U10m, SP, SO <sub>2</sub> , O <sub>3</sub> <sup>RA</sup>
3	T, MSLP, SP, T2m, CO, SO <sub>2</sub> , NO <sub>2</sub> , O <sub>3</sub> <sup>RA</sup>	T, U, DT2m, W, NO <sub>2</sub> , O <sub>3</sub> <sup>RA</sup>
4	U, U10m, MSLP, SP, T2m, SH, W, CO, NO, NO <sub>2</sub> , O <sub>3</sub> <sup>RA</sup>	-
5	U, U10m, MSLP, SP, T2m, W, CO, NO, NO <sub>2</sub> , O <sub>3</sub> <sup>RA</sup>	T2m
6	U, V, U10m, V10m, MSLP, SP, T2m, SH, CO, NO	-
7	U, U10m, MSLP, SP, T2m, SH, W, CO, NO, NO <sub>2</sub>	U, T2m
8	U, U10m, MSLP, SP, T2m, SH, W, CO, NO, NO <sub>2</sub> , O <sub>3</sub> <sup>RA</sup>	TCC, T2m
9	T, U, V, U10m, V10m, MSLP, SP, T2m, SH, W, CO, NO, NO <sub>2</sub>	-
10	T, U, U10m, MSLP, SP, T2m, W, NO, O <sub>3</sub> <sup>RA</sup>	TCC, FCC, U, V, U10m, V10m, MSLP, SP, T2m, DT2m, SH, SO <sub>2</sub> , NO, NO <sub>2</sub> , O <sub>3</sub> <sup>RA</sup>
11	U, U10m, MSLP, SP, T2m, W, CO, NO, NO <sub>2</sub> , O <sub>3</sub> <sup>RA</sup>	TCC, FCC, U, W
12	T, U, U10m, MSLP, SP, T2m, W, NO, NO <sub>2</sub> , O <sub>3</sub> <sup>RA</sup>	TCC
13	MSLP, SP, T2m, SH, W, NO, O <sub>3</sub> <sup>RA</sup>	-
14	T, U, U10m, MSLP, SP, T2m, SH, W, NO, O <sub>3</sub> <sup>RA</sup>	TCC, FCC, T2m, DT2m, SO <sub>2</sub> , O <sub>3</sub> <sup>RA</sup>
15	U, U10m, MSLP, SP, T2m, W, NO, O <sub>3</sub> <sup>RA</sup>	TCC, U
16	MSLP, SP, T2m, W, NO, O <sub>3</sub> <sup>RA</sup>	T, U, SP, W, O <sub>3</sub> <sup>RA</sup>
17	T2m, O <sub>3</sub> <sup>RA</sup>	-
18	T2m, SH, W, NO, O <sub>3</sub> <sup>RA</sup>	TCC, FCC, DT2m, W, O <sub>3</sub> <sup>RA</sup>
19	T, V10m, T2m, W, NO, O <sub>3</sub> <sup>RA</sup>	TCC, FCC, V10m
20	T, V, V10m, SP, T2m, SH, NO <sub>2</sub> , O <sub>3</sub> <sup>RA</sup>	TCC, SP, T2m, W, NO <sub>2</sub> , O <sub>3</sub> <sup>RA</sup>
21	T, V10m, T2m, W, CO, O <sub>3</sub> <sup>RA</sup>	CC, U, SP, SH, W, SO <sub>2</sub> , O <sub>3</sub> <sup>RA</sup>



22	T, V10m, MSLP, SP, T2m, W, O <sub>3</sub> <sup>RA</sup>	TCC, FCC, U, V10m, MSLP, SP, SH, O <sub>3</sub> <sup>RA</sup>
23	T, T2m, DT2m, W, O <sub>3</sub> <sup>RA</sup>	Q
24	T2m, O <sub>3</sub> <sup>RA</sup>	-
25	-	DT2m, CO
26	T, V, V10m, MSLP, SP, T2m, CO, O <sub>3</sub> <sup>RA</sup>	-
27	T, V, U10m, V10m, MSLP, SP, T2m, CO	-

690

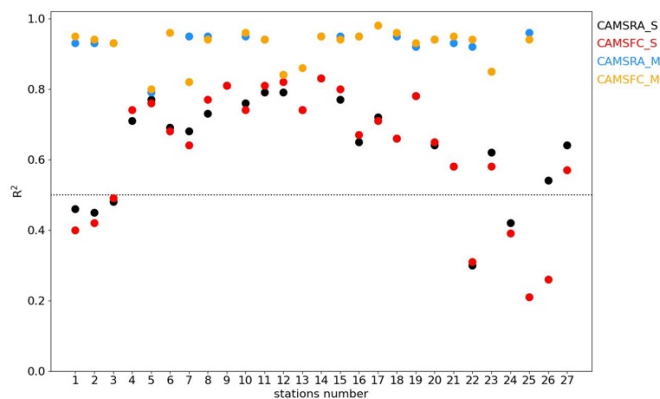
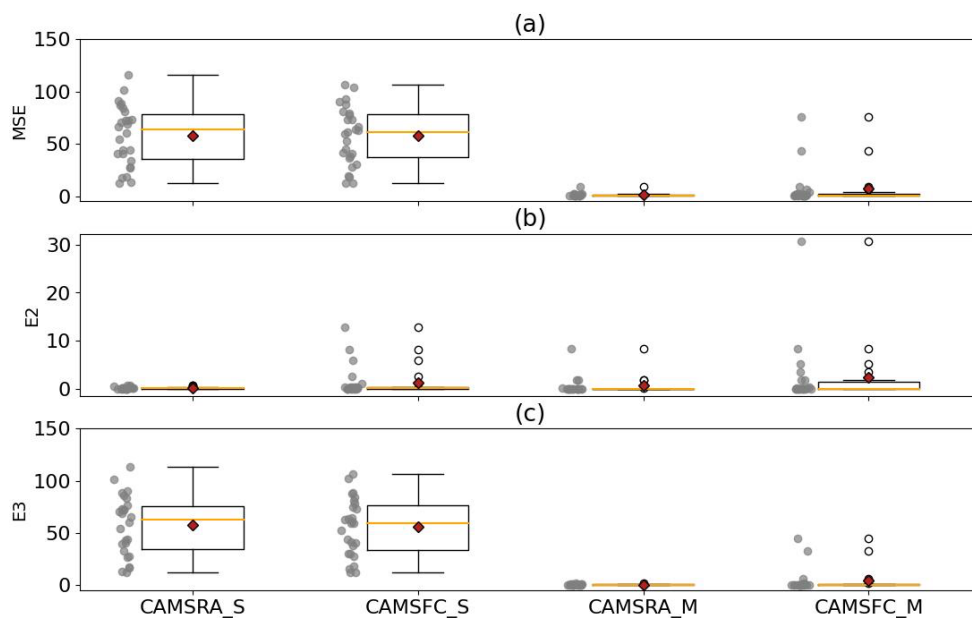


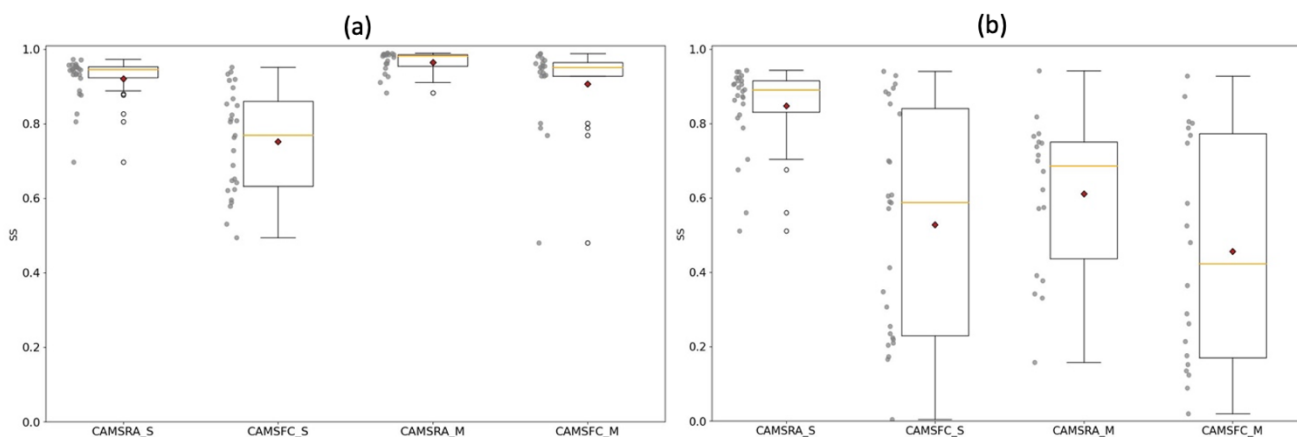
Figure 4. The  $R^2$  of the LSTM model for both S and M components of O<sub>3</sub>. In this figure, CAMSRA\_S and CAMSFC\_S refer to the S components of CAMSRA and CAMSFC, respectively. Likewise, CAMSRA\_M and CAMSFC\_M refer to the M component of CAMSRA and CAMSFC, respectively.

695



700

**Figure 5.** The (a) MSE, (b) E2, and (c) E3 of the downscaled  $O_3^{RA}$  and  $O_3^{FC}$  with LSTM for both S and M components. In this figure, CAMSRA\_S and CAMSFC\_S refer to the S components of CAMSRA and CAMSFC, respectively. Likewise, CAMSRA\_M and CAMSFC\_M refer to the M component of CAMSRA and CAMSFC, respectively.



705

**Figure 6.** The SS of the downscaled  $O_3^{RA}$  and  $O_3^{FC}$  with (a) LSTM and (b) LSTM<sup>no\_lag</sup>

710



## 715 Appendix A

**Table A1. The stations' names and their geographical locations**

Number	Name	Latitude	Longitude	Number	Name	Latitude	Longitude
1	Abresan (Tabriz)	38.066	46.326	15	Shad abad (Tehran)	35.67	51.297
2	Namaz square (Tabriz)	38.079	46.289	16	Mahallati (Tehran)	35.661	51.466
3	Azarbayej an square (Tabriz)	38.112	46.276	17	District 19 (Tehran)	35.635	51.362
4	Aqdasiyeh (Tehran)	35.795	51.484	18	Masoudieh (Tehran)	35.63	51.499
5	Sadr (Tehran)	35.778	51.429	19	Ray (Tehran)	35.604	51.426
6	District 2 (Tehran)	35.777	51.368	20	Hamedan (Hamedan)	34.8	48.5
7	Punak (Tehran)	35.762	51.332	21	Birjand (Khorasan Jonoubi)	32.87	59.21
8	Geophysics (Tehran)	35.74	51.385	22	Yazd manabeta biei (Yazd)	31.93	54.37
9	Setad bohran (Tehran)	35.727	51.431	23	Rasht (Gilan)	37.29	49.61
10	Tarbiat Modares (Tehran)	35.717	51.386	24	Zanjan ark (Zanjan)	36.67	48.48
11	Sharif university (Tehran)	35.702	51.351	25	Mirzaye shirazi (Markazi)	34.09	49.7
12	District 21 (Tehran)	35.698	51.243	26	Kazeroon gate (Shiraz)	29.61	52.53
13	Piroozi (Tehran)	35.696	51.494	27	Imam Hossein square (Shiraz)	29.62	52.54
14	Fath square	35.679	51.337				

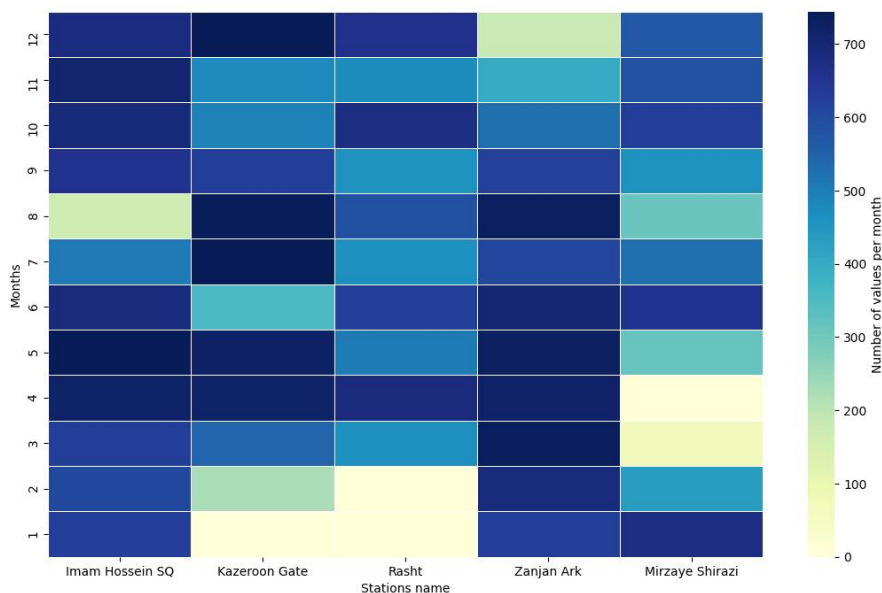


Figure A1. Data coverage (per month) of the hourly surface-based measured ozone at five air quality monitoring stations

725 Table A2. The hyperparameter settings of the LSTM model

hyperparameter	values
Train portion	65 %
Test portion	35 %
Epoch	1...30
Batch size	72
Optimizer	ADAM
Loss function	MSE

730

Table A3. A list of the meteorological variables that were extracted from CAMS data products.  $\oplus$  and  $\ominus$  present available and unavailable variables, respectively.

Meteorological variable (symbol)	Units	Definition	CAMSRA	CAMSFC
T	°K	Temperature	$\oplus$	$\oplus$
T2m	°K	2 meter temperature	$\oplus$	$\oplus$
SST	°K	Sea surface temperature	$\ominus$	$\oplus$
DT2m	°K	2 metre dewpoint temperature	$\oplus$	$\oplus$
SH	kg kg <sup>-1</sup>	Specific humidity	$\oplus$	$\oplus$



U	m s <sup>-1</sup>	U component of wind	⊕	⊕
V	m s <sup>-1</sup>	V component of wind	⊕	⊕
U10m	m s <sup>-1</sup>	10 meter U wind component	⊕	⊕
V10m	m s <sup>-1</sup>	10 meter V wind component	⊕	⊕
W	Pa s <sup>-1</sup>	Vertical velocity	⊕	⊕
BLH	m	Boundary layer height	⊖	⊕
SP	Pa	Surface pressure	⊕	⊕
MSLP	Pa	Mean sea level pressure	⊕	⊖
TCC	%	Total cloud cover	⊕	⊕
FCC	%	Fraction of cloud cover	⊕	⊕
UV	J m <sup>-2</sup>	Downward UV radiation at the surface	⊖	⊕
SD	s	Sunshine duration	⊖	⊕

735

Table A4. As Table 2, but for CAMSFC datasets.

Stations' number	S	M
1	DT2m, BLH, U10m, W, T, SH, NO <sub>2</sub> , NO <sub>x</sub> , CO	U, O <sub>3</sub> <sup>FC</sup>
2	BLH, W, T, U	U, SP, O <sub>3</sub> <sup>FC</sup>
3	BLH, T2m, U10m, W, T, U, O <sub>3</sub> <sup>FC</sup>	T, U, O <sub>3</sub> <sup>FC</sup>
4	BLH, V10m, V, O <sub>3</sub> <sup>FC</sup>	-
5	V10m, O <sub>3</sub> <sup>FC</sup>	O <sub>3</sub> <sup>FC</sup>
6	BLH, U10m, V10m, T, U, V, SP, O <sub>3</sub> <sup>FC</sup>	SST, SD
7	BLH, T2m, V10m, W, T, V, SO <sub>2</sub> , O <sub>3</sub> <sup>FC</sup>	O <sub>3</sub> <sup>FC</sup>
8	BLH, V10m, W, T, V, O <sub>3</sub> <sup>FC</sup>	SD, U, O <sub>3</sub> <sup>FC</sup>
9	BLH, T2m, V10m, W, T, V, NO, SO <sub>2</sub> , CO, O <sub>3</sub> <sup>FC</sup>	-
10	V10m, O <sub>3</sub> <sup>FC</sup>	BLH, T, O <sub>3</sub> <sup>FC</sup>
11	BLH, V10m, W, V, O <sub>3</sub> <sup>FC</sup>	SST, SD, O <sub>3</sub> <sup>FC</sup>
12	BLH, V10m, O <sub>3</sub> <sup>FC</sup>	O <sub>3</sub> <sup>FC</sup>
13	BLH, V10m, T, V, O <sub>3</sub> <sup>FC</sup>	O <sub>3</sub> <sup>FC</sup>
14	BLH, V10m, V, SP, NO <sub>x</sub> , SO <sub>2</sub> , CO, O <sub>3</sub> <sup>FC</sup>	DT2m, V10m, O <sub>3</sub> <sup>FC</sup>



15	T2m, V10m, O <sub>3</sub> <sup>FC</sup>	SD, BLH, O <sub>3</sub> <sup>FC</sup>
16	BLH, U10m, V10m, T, V, O <sub>3</sub> <sup>FC</sup>	DT2m, SST, BLH, T2m, U10m, V10m, W, T, U, V, SH, SP, NO, SO <sub>2</sub> , CO, O <sub>3</sub> <sup>FC</sup>
17	T2m, O <sub>3</sub> <sup>FC</sup>	BLH, V10m, O <sub>3</sub> <sup>FC</sup>
18	BLH, V10m, W, T, V, NO, O <sub>3</sub> <sup>FC</sup>	SD, T2m, U10m, V10mWu, V, NO <sub>2</sub> , NO, NO <sub>x</sub> , SO <sub>2</sub> , CO, O <sub>3</sub> <sup>FC</sup>
19	BLH, V10m, O <sub>3</sub> <sup>FC</sup>	TCC, O <sub>3</sub> <sup>FC</sup>
20	DT2m, BLH, T2m, U10m, T, U, SH, O <sub>3</sub> <sup>FC</sup>	TCC, BLH, W, Q, SP, O <sub>3</sub> <sup>FC</sup>
21	BLH, V, SO <sub>2</sub>	BLH, T, SP, SO <sub>2</sub> , CO, O <sub>3</sub> <sup>FC</sup>
22	DT2m, SD, BLH, T2m, U10m, V10m, W, T, U, V, SH, SP, NO <sub>2</sub> , CO, O <sub>3</sub> <sup>FC</sup>	BLH, U10m, SH, SP, SO <sub>2</sub>
23	U10m, O <sub>3</sub> <sup>FC</sup>	Q
24	T2m, O <sub>3</sub> <sup>FC</sup>	-
25	BLH	DT2m, SST, BLH, O <sub>3</sub> <sup>FC</sup>
26	BLH	-
27	SP	-

740

**Table A5. The optimum epoch number to perform the LSTM model**

models	CAMSRA		CAMSFC	
	S	M	S	M
Stations' number	S	M	S	M
1	27	26	28	26
2	26	26	29	26
3	27	20	27	26
4	26	-	26	-
5	27	25	26	26
6	27	-	26	26
7	27	26	28	26
8	27	26	26	26

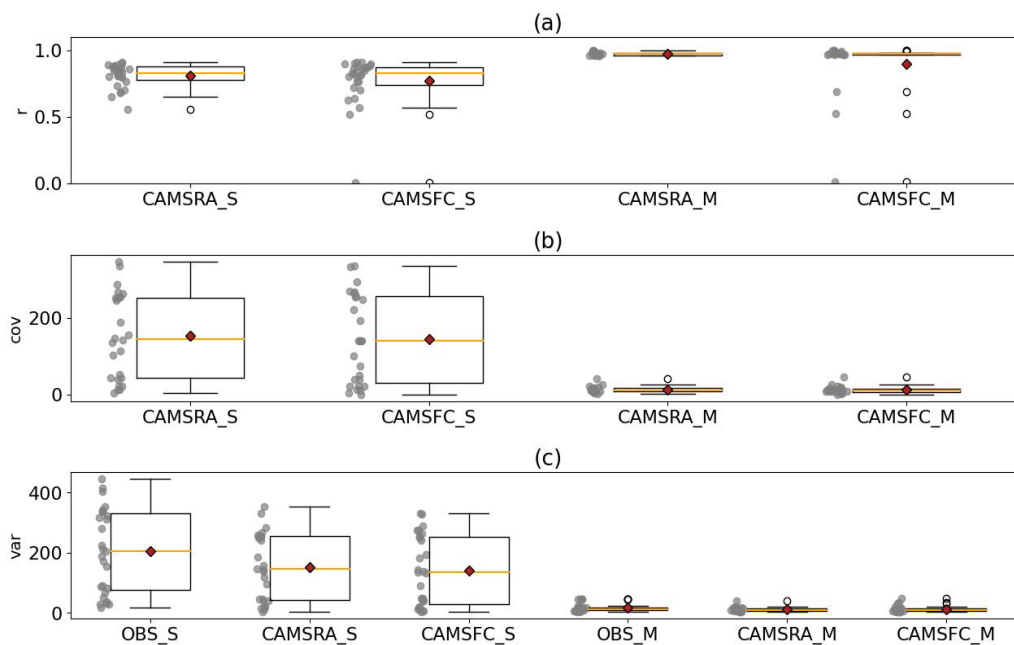


---

9	30	-	27	-
10	30	22	30	26
11	27	26	27	26
12	27	25	26	26
13	27	-	30	26
14	27	26	26	26
15	28	26	26	27
16	26	26	25	26
17	26	-	26	26
18	30	26	27	26
19	26	26	26	26
20	26	26	28	26
21	26	27	26	26
22	26	28	27	26
23	30	26	26	26
24	7	-	7	-
25	-	26	25	24
26	26	-	25	-
27	27	-	25	-

---





750 **Figure A2.** The (a) correlation ( $r$ ), (b) covariance ( $cov$ ), and (c) variance ( $var$ ) of the  $O_3^{SD}$  with LSTM.

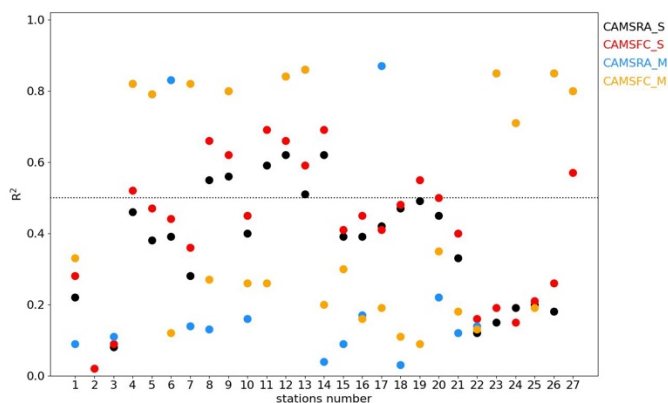
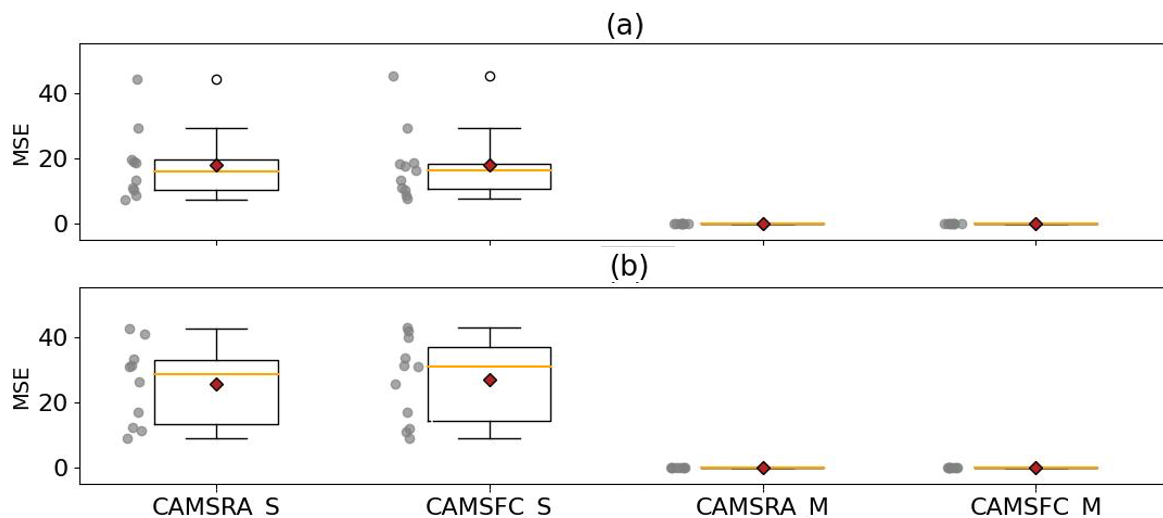


**Figure A3.** As Fig. 4, but for the LSTM<sup>no\_lag</sup> model.

755



Figure

A4. The MSE of the  $O_3^{SD}$  at the stations (excluding the stations over Tehran city) for (a) the cold {months = 1 to 3, and 10 to 12} and (b) the warm {months = 4 to 9} seasons, respectively.

760

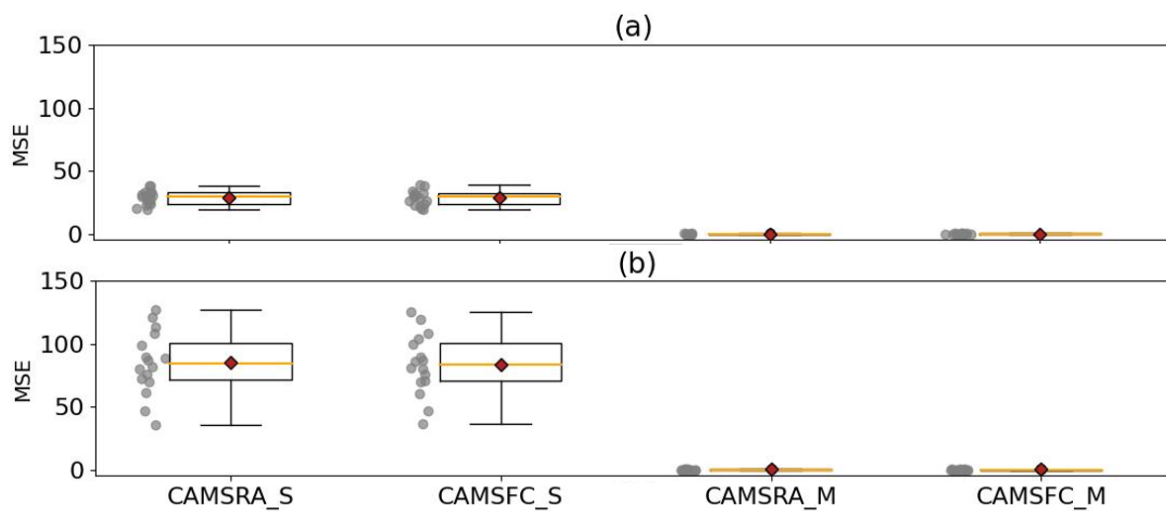
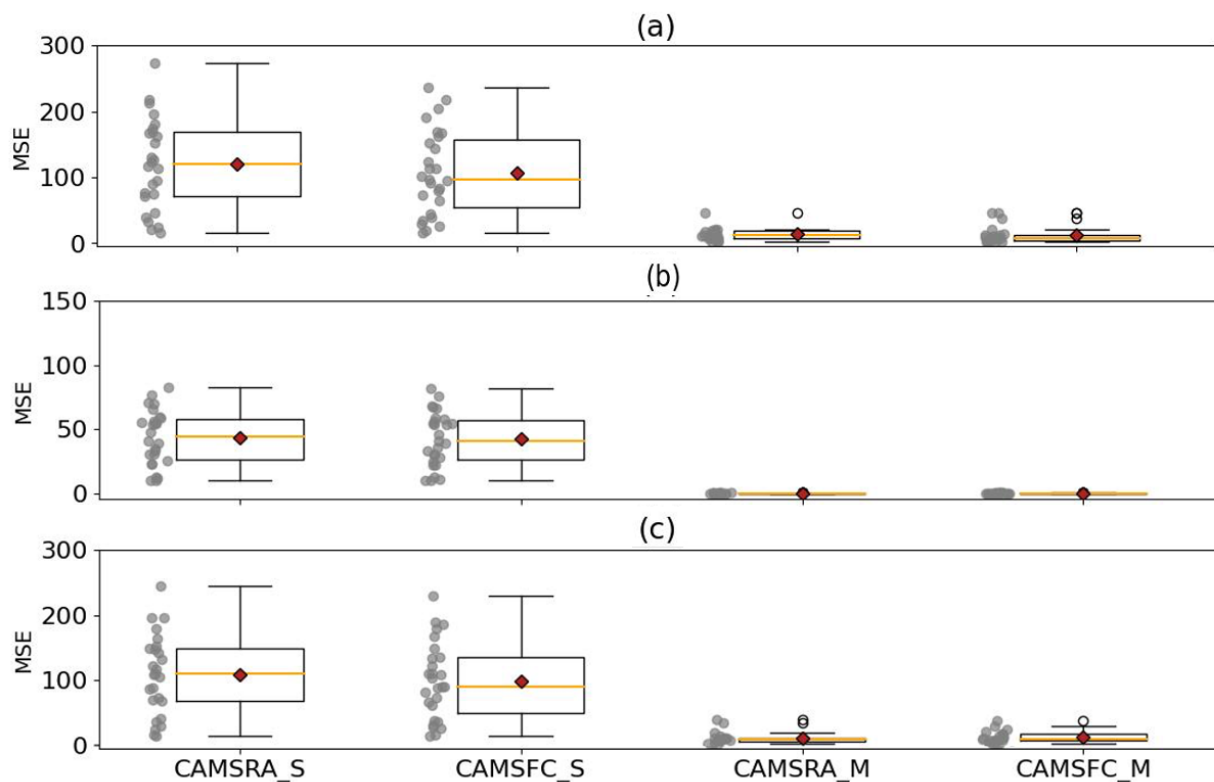
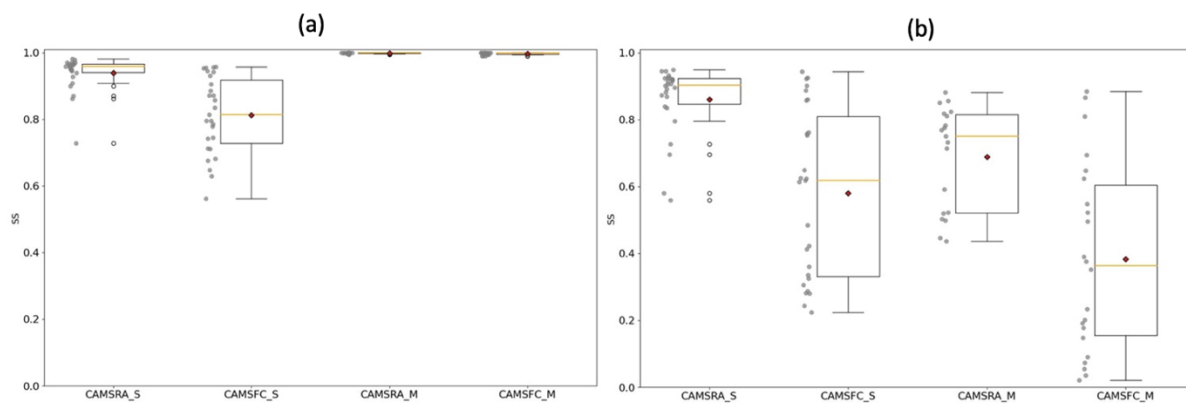


Figure A5. The MSE of the  $O_3^{SD}$  at the stations over Tehran for (a) the cold {months = 1 to 3, and 10 to 12} and (b) the warm {months = 4 to 9} seasons.

765



770 **Figure A6.** The MSE of the  $O_3^{SD}$  by the (a)  $LSTM^{no\_lag}$ , (b) MLR, and (c)  $MLR^{no\_lag}$  models



775 **Figure A7.** As Fig. 6 but for the downscaled data with (a) MLR and (b)  $MLR^{no\_lag}$  models.